

RESEARCH ARTICLE | MARCH 21 2017

Thermokinematic memory and the thixotropic elasto-viscoplasticity of waxy crude oils

Special Collection: [Virtual Issue on Thixotropy](#)

Michela Geri; Ramachandran Venkatesan; Krishnaraj Sambath; Gareth H. McKinley



J. Rheol. 61, 427–454 (2017)

<https://doi.org/10.1122/1.4978259>



View
Online



Export
Citation

Related Content

A 1.5D Numerical Model for Weakly Compressible Viscoplastic and Thixotropic Flows: Application to the Start-up of Waxy Crude Oils in Pipeline

AIP Conf. Proc. (July 2008)

Thixotropy and rheological hysteresis in blood flow

J. Chem. Phys. (February 2022)

A multimode structural kinetics constitutive equation for the transient rheology of thixotropic elasto-viscoplastic fluids

J. Rheol. (January 2018)



Thermokinematic memory and the thixotropic elasto-viscoplasticity of waxy crude oils

Michela Geri^{a)}

Department of Mechanical Engineering, Massachusetts Institute of Technology, Cambridge, Massachusetts 02139

Ramachandran Venkatesan and Krishnaraj Sambath

Chevron Energy Technology Company, Houston, Texas 77002

Gareth H. McKinley

Department of Mechanical Engineering, Massachusetts Institute of Technology, Cambridge, Massachusetts 02139

(Received 6 July 2016; final revision received 22 February 2017; published 21 March 2017)

Abstract

The effect of thermal and shear history on the rheology of waxy crude oils is studied in detail. A protocol sequence is presented, which enables us to systematically extract the main thixotropic features of a model waxy oil by a series of steady state and transient experiments at different temperatures. The importance of the underlying microstructure formed by a loosely aggregated and percolated network of wax crystals is discussed and quantified through differential scanning calorimetry and rheological measurements. The microstructural morphology can be described by relevant concepts used previously in the literature for concentrated suspensions of fractal aggregates and is augmented with evolution equations to capture the transient rearrangement of the microstructure, resulting in a thermokinematic memory of the shearing history and thermal history of the sample. Finally, a complete constitutive framework is derived that is able to quantitatively describe and predict a number of rheological features of the model waxy oil, such as viscoelasticity at small deformations and plasticity at large deformations, with both the yield stress and viscosity exhibiting thermokinematic memory. Direct comparison with rheometric data is used to determine the model constants and evaluate the predictive ability of the constitutive relations. The proposed model provides a new framework that can be used to describe not only waxy crude oils, but also other materials characterized by similar microstructural components, i.e., solid non-Brownian interacting particles of arbitrary shape that form a percolated sample-spanning network and convey thixotropy as well as elasto-viscoplasticity. © 2017 The Society of Rheology. [http://dx.doi.org/10.1122/1.4978259]

I. INTRODUCTION

Many materials that belong to the broad category of complex fluids can be described from a continuum mechanical prospective as *elasto-viscoplastic* (EVP) materials [1–5]. With this term, we refer to any substance that displays finite viscoelastic solidlike behavior at small deformations but flows plastically at large deformations when a critical stress value is exceeded. It is widely recognized, however, that the plastic behavior of many complex fluids also shows a time dependent evolution of the yield stress and the plastic viscosity known as *thixotropy* [6–10]. Thus more generally, EVP materials that show a shear history dependence of their flow properties, or what can be called more broadly a *kinematic memory*, can be referred to as *thixotropic EVP* (TEVP) materials.

The interest in TEVP fluids has increased over time since thixotropy was first recognized about a century ago [6], primarily due to the multitude of industrial materials that show this behavior [8]. Food products, pharmaceuticals, coatings,

inks, paints, and crude oils all fall into the category of TEVP materials [11]. From an experimental point of view, there are a number of protocols that have been developed and widely used to study the rheological behavior of such materials. These tests are mainly based on hysteresis loops, shear rate steps, creep tests, start up of shear flow, and recently also large amplitude oscillatory shear (LAOS) tests [8,9,12,13]. From a theoretical point of view, prolific activity has resulted in a number of viable models that capture specific features experimentally observed in particular materials [8,14]. Among these, a great number can be reduced to the class of *structural kinetics models* [15]. They are based on the idea that complex fluids are characterized by a dispersed phase, be it solid particles (suspension), liquid droplets (emulsion), or gas (foam), and that the macroscopic rheological behavior is directly coupled to the microscopic rearrangements of the material structure that arise from interactions and reorganization of the constituents of the dispersed phase [7,9,16]. To capture, in an approximate way, the rearrangements of this microstructure, a single *structural parameter* is typically introduced (often generically indicated by the Greek letter λ) that evolves as a function of time and level of deformation [8,17,18]. Among such models, one can in general find two broad classes [14]: one that comprises constitutive equations

^{a)}Author to whom correspondence should be addressed; electronic mail: mgeri@mit.edu

developed from a Binghamlike plastic response [13,15] and the other one that includes constitutive equations derived from extensions of existing viscoelastic models [11,19]. Recently, Larson [20] has pointed out that not all the constitutive equations belonging to this class are indeed thixotropic in nature. He shows that many of them are actually only complex nonlinear viscoelastic models with different relaxation time scales and argues toward a necessary distinction between nonlinear viscoelasticity and *nonideal thixotropy*, i.e., thixotropy coexisting with viscoelasticity, both in assessing the rheological behavior [9] and in developing constitutive equations.

A very different approach has been taken by other researchers who have addressed the problem by modeling directly the interactions among microstructural constituents. Different perspectives have given rise to a number of frameworks; some of the most popular include the soft glassy rheology (SGR) model [21,22], the shear transformation zone (STZ) model [23,24], and the kinetic elastoplastic (KEP) model [25,26]. Although these models are able to capture several features that have been observed in real materials [27,28], they are usually more difficult to use because the measurable macroscopic quantities, such as stress or viscosity, are not directly involved in the model formulation and need to be computed based on other microscopic variables that are specific to the different models. As a consequence, direct comparison with experiments and determination of material parameters becomes computationally more expensive and less suitable for being used in engineering applications such as the optimization of flow assurance strategies [29,30].

A particular subset of TEVP materials that differs from most of the others is represented by waxy crude oils (WCOs). The rheological behavior of these materials is known to be strongly affected not only by the shear history to which they are subject to but also by their thermal history [31]. The size, shape, and connectivity of the wax crystal aggregates exhibit a form of *thermokinematic memory*, which is responsible for a very complex rheological behavior, most of which has not been fully understood yet [32], notwithstanding the consistent effort that has been devoted over a number of years [29,31,33]. The ability to quantify the rheological characteristics of different WCOs is crucial for oil production, especially when dealing with off-shore deepwater fields and marginal fields [30,34]. The large changes in temperature and pressure that arise during these production scenarios result in the formation of several different solid precipitates, including clathrate hydrates, waxes, and asphaltenes, depending on the original composition of the oil [35]. The microstructural state of these precipitates can then evolve with the shearing and thermal history profile experienced by the material elements flowing along the pipe. Paraffinic components are one of the biggest issues that can affect resource extraction [32], with negative consequences in terms of both production and environmental cost due to pipeline blockages that reduce the extraction rate and increase the risk of equipment damage. Paraffin wax is usually dissolved in the oil phase at the well head, but as the temperature of the crude oil decreases below a critical value known as the wax appearance temperature (WAT), its

solubility decreases and precipitation is thermodynamically favored [36,37]. The presence of solid wax crystals is responsible for changes in the rheological behavior of WCOs even at very small concentrations (about 2%) [38,39], transforming the oil from a simple Newtonian fluid to a TEVP fluid with the thermokinematic memory described above. However, little is known about the mechanisms that lead to these changes and how we can account for them systematically in a constitutive model that can be used to safely and economically assure production, i.e., to devise flow assurance strategies even in fields that operate under critical conditions [29,40–42].

Extensive effort has been devoted to investigating the different features that can be experimentally observed in many crude oils [43]. Working with real crude oils though can be very challenging because their composition is extremely variable depending on their origin [44], and deconvolving the effects of different components that may precipitate together with paraffins can make the interpretation of experimental results very difficult [45]. For this reason, many researchers have preferred to work with model waxy oils that are specifically formulated to contain only paraffinic compounds, but that still retain most of the rheological signatures observed in real WCOs, and which make them TEVP materials [46–48]. Nonetheless, their thermokinematic memory has, until recently, hindered the ability of obtaining reproducible experimental results, which can be fully understood [48,49].

From a theoretical point of view, many proposed models still have considerable limitations in terms of capturing the different aspects of the TEVP nature of WCOs. The most widely used is the Houska model [50], which is not only inelastic but also isothermal. Pedersen and Rønning [51] have proposed a temperature-dependent model for the plastic viscosity based on the wax volume fraction, which, although inelastic, captures through fitting some of the most important characteristics at high shear rates such as shear thinning. Visintin *et al.* [52] have also considered the importance of the wax volume fraction and proposed equations for the viscoelastic moduli and for the plastic viscosity with functional forms derived from the observed experimental trends. Recently, Palermo and Tournis [53] have revisited some of the older correlations commonly used in the oil industry for the viscosity of waxy oils and they have proposed a new model based on previous work done in the context of concentrated attractive suspensions [54] which they call the suspension of fractal aggregates (SoFA) model. The SoFA model is also inelastic and introduces empirical correlations for its three parameters which do not reflect specific physical processes; however, it does consider the importance of the temperature history through an evolution in the effective volume fraction of precipitated wax $\phi_e(T)$, a concept that we will revisit below. Mendes *et al.* [55] have also proposed a model in which the material is considered to be viscoelastic below a yield stress, that is determined based on a critical shear strain, and that flows plastically above that threshold with a viscosity which evolves in time based on the shear rate and the total shear strain. This isothermal one-dimensional model introduces 11 parameters; a separate set of equations that include temperature are provided for the

equilibrium flow curves, obtained after the material has undergone a specific thermal and shear history.

Dimitriou and McKinley [49,56] have recently proposed a constitutive equation based on the frame invariant and thermodynamically consistent framework of TEVP models used in continuum mechanics [57–59]. Their isotropic kinematic hardening (IKH) model was demonstrated to capture many salient features of a model waxy oil, including the steady state flow curve, the stress overshoot in startup of steady shear and LAOS tests. However, the IKH model does not account for different shear or thermal histories and is limited to properly explaining isothermal experimental results, only after a certain preshearing protocol has been applied.

In the present work, we wish to expand our understanding of the complex behavior observed in WCOs by developing a comprehensive constitutive framework that accounts for the thermokinematic history of these TEVP materials. To this end, we propose a set of experimental protocols designed to highlight the rheological complexities of a model WCO, and we use these experimental observations to guide the development of a constitutive equation that can quantitatively predict the rheological response of the model waxy oil. We discuss the assumptions made and their connection to physical mechanisms that take place during deformation and flow of WCOs. Direct comparison with experiments confirms the ability of this constitutive framework to quantitatively capture viscometric data. In addition, the model developed can be generalized to a three-dimensional, frame invariant and thermodynamically consistent form based on the well known Kröner–Lee decomposition of the deformation gradient commonly used in continuum mechanics [59]. Given the generality of our treatment, we believe that the proposed framework is broadly applicable to simulations of complex flows for a wide range of thixotropic and EVP materials.

II. RHEOLOGICAL CHARACTERIZATION

WCOs exhibit a wide range of complex thermorheological behaviors below their WAT. They are viscoelastic solids when deformed within the linear region, but flow plastically at sufficiently large deformations [38,39,47–49,55,56]; their yielding process is characterized by different mechanisms of hardening and softening that are common in more solidlike materials such as metals or metallic glasses [56,57,59]. In addition, their thermokinematic memory makes them strongly thixotropic as a consequence of both their previous shearing and thermal histories [40,52,60]. Substantial progress has recently been achieved in the development of suitable experimental protocols as well as viable constitutive models that are able to capture some of the essential rheological features [49,55,56,61]. However, this progress has been restricted to the case when a given thermokinematic preconditioning (i.e., so called “thermal beneficiation” and “shear rejuvenation”) has been applied so that the rheological response is readily reproducible.

In order to overcome these limitations, we describe a series of experimental protocols to study more completely the effect of shearing and thermal history on the rheological

behavior of WCOs. The experiments first investigate the effect of temperature on the viscosity of the oil. Subsequently, attention is paid to two distinct thixotropic aspects: The tendency of the viscosity to evolve over a significant time scale when subject to a constant shear rate under isothermal conditions and the thermokinematic memory of the sample, which is manifested by the material response depending on the maximum shear rate that the sample has ever experienced at that temperature. This last characteristic has recently been reported in flow curve measurements of a real crude oil by Mendes *et al.* [55] but has also been observed previously in different forms by other researchers [39,40,52].

A. Materials and methods

Working with real crude oils can be challenging because their composition is extremely variable depending on their origin [44]. To focus the attention on wax precipitation, in this work we use a model waxy oil made of a combination of a heavy mineral oil (Sigma Aldrich, 330760) and a paraffin wax with melting point between 58 and 62 °C (Sigma Aldrich 327212, ASTM D 87). This formulation has been successfully used before as a model WCO [47,56]. In our experiments, the total wax concentration has been maintained constant and is equal to 10 wt %. As will become clearer in Sec. III, this does not represent a serious limitation for the study. The mixture is prepared by adding the solid wax to the oil at room temperature in a glass container that is subsequently transferred to a hot plate equipped with a magnetic stirrer. The mixture is stirred while keeping the material at a temperature well above the WAT, usually around 80 °C. The rheological WAT for this particular composition has been measured to be $T_{wa} = 37$ °C (see Fig. 2 below). The mixture is kept on the hot stirring plate for about an hour to ensure that the melted wax is homogeneously distributed throughout the oil phase. Samples used in the experiments have been prepared at different times with the same method and composition, using the same batch of paraffin wax. Working with the same wax is important to obtain reproducible results, given the variability in paraffinic composition that can be found even within such a small range of melting temperatures.

The experiments are performed on a stress controlled rheometer (TA Instruments, DHR-3). The geometry used is a 60 mm, 2 °C cone with truncation gap of 58 μm. The bottom plate is a standard Peltier plate with a platinum resistance thermometer sensor placed at the center which ensures a precise temperature measurement and control (± 0.1 °C). Because of the tendency of WCO to slip on solid surfaces [47,56], both the cone and the plate surface were roughened by applying an adhesive-backed waterproof sandpaper with nominal average surface roughness $R_a = 25$ μm. Although the material is not prone to evaporative losses, a single sample has not been used for more than 48 h of continuous measurements. A new application of sandpaper is also performed at each change of sample, along with a recalibration of the instrument and geometry. Care is taken to ensure that the

sandpaper does not introduce additional noise in the torque signal bigger than the instrumental noise floor.

The experimental protocols used in the present study can be generalized into a particular set of steps as shown in Fig. 1.

- (1) Beneficiation step [51], performed by applying steady shear at $\dot{\gamma} = \dot{\gamma}_{cool}$ at a temperature $T_i = 60^\circ\text{C}$ (well above the WAT) to erase any previous shearing history of the sample. This step is performed for a time $t_1 = 10\text{ min}$.
- (2) Temperature ramp from T_i down to a variable final temperature T_f at a constant cooling rate $\dot{T} = -1^\circ\text{C}/\text{min}$ and constant shear rate $\dot{\gamma} = \dot{\gamma}_{cool}$. The length of this step varies with T_f since $t_2 - t_1 = (T_f - T_i)/\dot{T}$. The cooling rate is kept constant throughout the experiments while T_f has been varied over the interval 40–50 °C.
- (3) Shear rejuvenation step [62], from t_2 to t_3 , performed by shearing the sample at the final temperature T_f and at constant shear rate $\dot{\gamma} = \dot{\gamma}_{cool}$. It has been shown in previous works [56] that this step is fundamental as a preconditioning stage in order to obtain reproducible results in experiments with WCOs as well as with other materials [62]. The transient response of the sample to this step is of great importance and is examined in more detail in Sec. II B 2.
- (4) Shear rate sweep at the final temperature T_f from $\dot{\gamma}_{max} = 500\text{ s}^{-1}$ to $\dot{\gamma}_{min} = 0.01\text{ s}^{-1}$ to obtain the equilibrium flow curve at the chosen temperature. At each point, the material is allowed to equilibrate for up to 5 min and the final stress value reported is an average of the last three instrumental measurements (performed at intervals of 30 s) that differ by less than 5%. The sweep is always run from high to low shear rates so that when conducting the measurement at the smallest shear rates the sample has already accumulated a very large total shear strain.

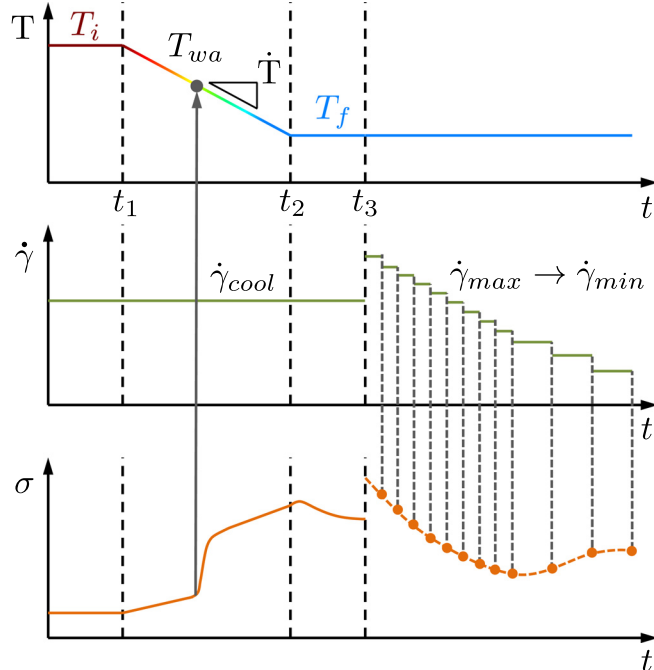


FIG. 1. Schematic of the implemented experimental protocol as described in Sec. II A. From top to bottom: Imposed temperature, imposed shear rate, and the resulting measured shear stress.

In the experiments, $\dot{\gamma}_{cool}$, $\dot{\gamma}_{max}$, and T_f have been varied in order to probe different rheological features of the model waxy oil. Explicit values will be specified in the appropriate sections.

B. Experimental results and discussion

We discuss the characteristics of the model waxy oil by examining different aspects of its rheological behavior. As anticipated above, first we consider the effect of temperature. To this end, the experimental protocol described in Sec. II A has been implemented, keeping constant both the shear rate during cooling ($\dot{\gamma}_{cool} = 50\text{ s}^{-1}$) and the maximum shear rate used in measuring the flow curve ($\dot{\gamma}_{max} = 500\text{ s}^{-1}$). Multiple experiments have been performed by varying the final temperature T_f from 40 to 5 °C.

Next, to study the effect of the maximum shear rate experienced by the material, the same protocol has been implemented but keeping the final temperature constant ($T_f = 26^\circ\text{C}$, $T_f/T_{wa} = 0.96$) and varying $\dot{\gamma}_{max}$. For this set of experiments, $\dot{\gamma}_{cool}$ has been set equal to $\dot{\gamma}_{max}$ and varied accordingly. This allows us to explore an interesting behavior of the model oil that can be observed during the rejuvenation step, namely, the evolution of the shear stress and viscosity over time at constant temperature and shear rate.

1. Effect of temperature

Figure 2(a) shows the characteristic increase in viscosity with decreasing temperature measured at constant applied shear rate ($\dot{\gamma} = 50\text{ s}^{-1}$, $T_f = 5^\circ\text{C}$, step 2 of the experimental protocol). The mineral oil/paraffin wax mixture displays an Arrhenius dependence ($\Delta H/R = 3.61 \times 10^3\text{ K}$), equivalent to the Andrade expression [63,64], for temperatures above the WAT. For $T \simeq T_{wa}$, the trend deviates from exponential with a sharp additional increase in viscosity that persists until the temperature reaches approximately 10 °C, at which point Arrhenius behavior is observed again, but with a higher apparent activation energy ($\Delta H/R = 4.57 \times 10^3\text{ K}$). Qualitatively, this trend in $\eta(T)$ is a feature that is common to numerous different model waxy oils as well as real crude oils [32,40,56,65]. It is worth noticing that although the viscosity increases quite sharply close to the WAT, its variation is still low enough that viscous heating effects can be neglected everywhere. This can be easily seen by estimating the Nahme–Griffith number defined as $Na = \eta V^2/k\Delta T$, where in our case the velocity is a function of the gap size and shear rate ($V = H\dot{\gamma}$) and the relevant temperature difference can be expressed as $\Delta T \sim \eta/(\partial\eta/\partial T)$. For the model WCO, the thermal conductivity k is of the order of $10^{-1}\text{ W}/(\text{m K})$, the velocity varies based on the shear rate but at most can reach a value $\mathcal{O}(10^{-1}\text{ m/s})$, and the variation of viscosity with temperature is at most (close to the WAT) of order 10^{-2} Pa s/K . Based on these values, an estimate of the Nahme–Griffith number gives $Na \sim 10^{-3}$, which is indeed much smaller than unity, meaning that thermal conductivity dominates over viscous dissipation.

Figure 2(b) shows a series of flow curves (shear stress versus shear rate) for the model oil as a function of temperature (step 4 of the experimental protocol). To improve the

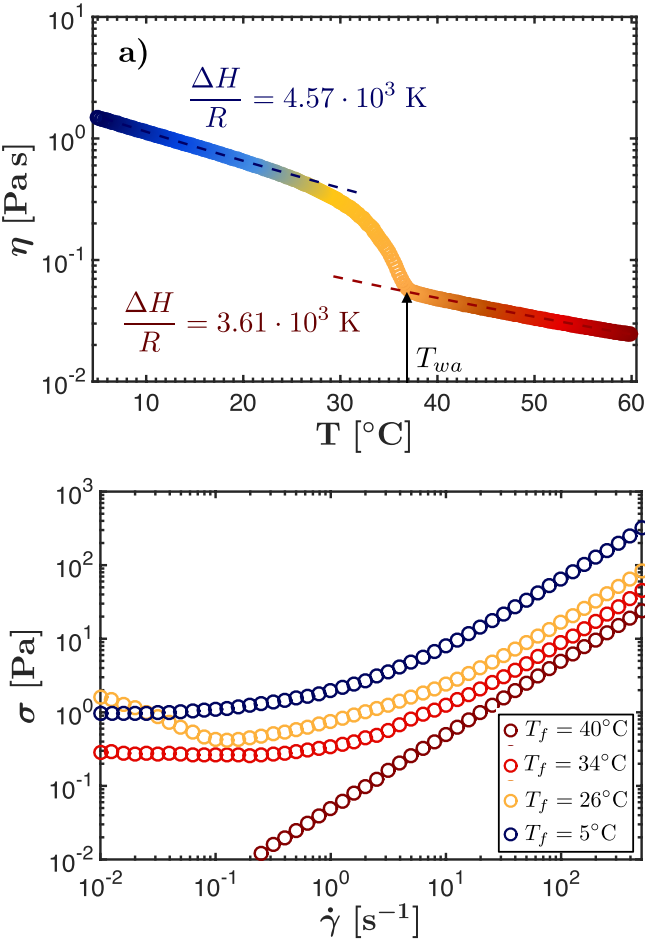


FIG. 2. Results from the experimental protocol of Fig. 1 with $\dot{\gamma}_{cool} = 50 \text{ s}^{-1}$ and $\dot{\gamma}_{max} = 500 \text{ s}^{-1}$. (a) Temperature ramp (step 2 of the experimental protocol) for a 10 wt. % paraffin wax in heavy mineral oil from $T_i = 60^\circ\text{C}$ to $T_f = 5^\circ\text{C}$ at $\dot{\gamma}_{cool} = 50 \text{ s}^{-1}$ and $\dot{T} = -1^\circ\text{C}/\text{min}$. The rheological WAT (T_{wa}) is defined as the value at which the viscosity increase deviates from the exponential Arrhenius form, in this case $T_{wa} \simeq 37^\circ\text{C}$; (b) flow curves (step 4 of the experimental protocol) at different final temperatures (T_f) as specified in the legend. The trends show that when $T > T_{wa}$ the mixture behaves as a Newtonian liquid with constant viscosity. As the temperature is lowered below T_{wa} , the material maintains its Newtonian nature only at very high shear rates, below which first shear thinning and then a complex yielding behavior develop.

plot legibility only four temperatures are displayed (see Appendix A for a plot with all the temperatures investigated). At $T = 40^\circ\text{C}$ the temperature is still above the WAT for this composition, no wax has precipitated out of solution and the behavior of the mixture is purely Newtonian as expected. As the temperature is lowered below the WAT, the flow curves show the complex rheological signature previously reported in the literature [48,56]. At high shear rates (above 100 s^{-1}), the response can be considered Newtonian with a plastic viscosity that is essentially constant; at intermediate shear rates, the decreasing slope of the stress/strain rate trend hints at a shear thinning behavior; and finally at the lowest shear rates the material passes through a minimum in the shear stress, often referred to as *dynamic yield stress* (σ_{dy}) [33]. Below this point, there is a decreasing branch where the shear stress decreases as the shear rate increases. The nonmonotonic trend is more pronounced over the range of temperatures that falls about $10\text{--}20^\circ\text{C}$ below WAT. It is

known [66,67] that such decreasing branches represent an intrinsically unstable region for any type of flow, including simple Couette flow such as that realized in a cone and plate geometry [68]. The most common instabilities that occur under these circumstances, and that have reportedly been observed in many complex fluids, are shear banding [67,69–74] and slip [75–77]. It goes beyond the scope of this work to establish the importance of each of these issues for the model WCO. However, we have performed complementary experimental studies that make use of ultrasound speckle velocimetry (USV) in a customized Taylor Couette geometry to resolve the local flow kinematics that develops in the nonmonotonic branch and will report on this separately [78]. In the context of the present work, we focus our attention on the region where the flow is hydrodynamically stable, that is, in the monotonic region of the flow curve, for stress above and including the dynamic yield stress.

With these observations in mind, it is interesting to note from Fig. 2(b) that the behavior of the waxy oil shows qualitatively similar trends at all temperatures. Each flow curve has the same type of functional dependence of the stress on the shear rate, although for decreasing temperatures, as the composition of the waxy oil changes, the magnitude of the measured stress at each shear rate increases. This behavior highlights the importance of understanding the relationship between temperature and the amount of precipitated wax [40].

2. Time dependent behavior: Stress evolution under steady shear

As anticipated above, an important thixotropic response to analyze is the stress evolution during shear rejuvenation (step 3 in the experimental protocol). In this case, the experiments have been performed at constant final temperature $T_f = 26^\circ\text{C}$ changing only the value of shear rate during cooling and rejuvenation, maintaining $\dot{\gamma}_{cool} = \dot{\gamma}_{max}$. This way the material is never subject to a shear rate greater than $\dot{\gamma}_{max}$ and it is possible to analyze what happens when changing this value.

Figure 3(a) shows a comparison of all the rejuvenation steps performed under different shear rates. For a purely Newtonian fluid, once a certain temperature has been reached, the viscosity (and therefore the resulting shear stress) should remain constant under a constant applied shear rate. The same should apply for an ideal yield stress fluid. However, in the present case, we clearly observe that the stress measured during this step keeps decreasing monotonically toward a steady state value that is reached faster at higher shear rates. This time dependent behavior is, by definition, the fingerprint of thixotropy or, more precisely, a hallmark of *thixo-viscous* behavior (as defined by Larson [20]). Although the same behavior is observed at any of the shear rates studied and is very reproducible, there has been no successful attempt so far to rationalize this empirically observed trend. We will see in Sec. IV A 2 that this response is inherently consistent with other features observed experimentally and can be explained in the same theoretical context.

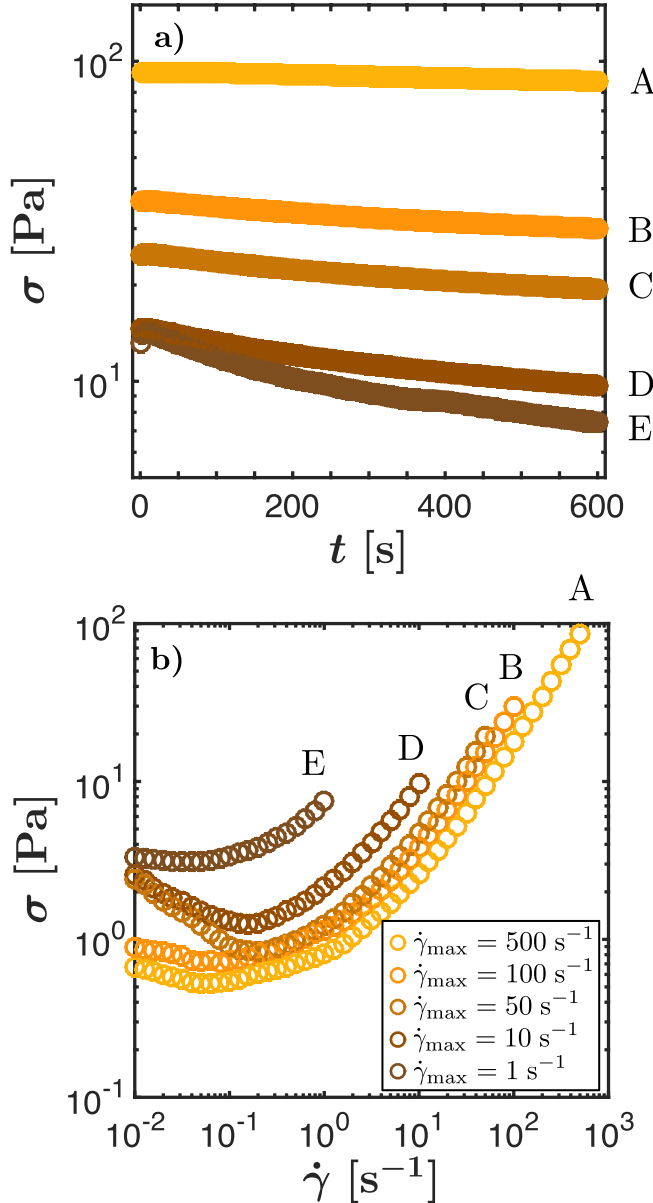


FIG. 3. Results from the experimental protocol of Fig. 1 with $T_f = 26^\circ\text{C}$ ($T_f/T_{wa} = 0.96$) and $\dot{\gamma}_{cool} = \dot{\gamma}_{max} = 500, 100, 50, 10, 1 \text{ s}^{-1}$, respectively. (a) Time evolution of the stress during the shear rejuvenation step [step 3 of the experimental protocol]. Legend the same as in (b)]. The stress does not achieve a constant value immediately after the temperature ramp but shows a long slow monotonic decay toward a steady state value for all the shear rates investigated; (b) flow curves (step 4 of the experimental protocol) measured after the rejuvenation step shown in part (a). For each curve, the entire protocol has been repeated, changing only $\dot{\gamma}_{max}$.

3. Irreversible destructuring: Effect of maximum shear rate

Figure 3(b) summarizes the flow curves that have been measured following the shear rejuvenation steps of Fig. 3(a). Each curve has been obtained after repeating the experimental protocol described in Sec. II A using the same final temperature ($T_f = 26^\circ\text{C}$), but changing the maximum shear rate used in the shear rate sweep and during cooling ($\dot{\gamma}_{max} = \dot{\gamma}_{cool}$). The effect on the flow curve is quite pronounced, with the stress measured for a given shear rate being reduced by as much as one order of magnitude as $\dot{\gamma}_{max}$ is increased from 1 to 500 s^{-1} . This memory of the maximum shear rate resembles that

observed for a change in temperature [cf. Fig. 2(b)] although the similarity is, in a sense, since the composition of the model waxy oil (i.e., the amount of wax ultimately precipitated at a temperature $T_f < T_{wa}$) is expected to be the same for all of the curves in Fig. 3(b). Previous works [39,55] suggest that the change generated in the material by increasing the maximum shear rate is irreversible. Once the sample has been exposed to a higher $\dot{\gamma}_{max}$, its response is permanently shifted unless a thermal beneficiation step is performed (if the sample is heated back to a temperature well above the WAT, then any previous history is erased; this corresponds to step 1 in the experimental protocol). A partial recovery can be obtained if the material is left to age for a sufficiently long period of time [39] although longer experiments will be required to definitively prove the response after any transient has died out. The results shown in Fig. 3(b) and the comparison with Fig. 2(b) suggest that not only the amount of precipitated wax is important in defining the rheological response of the model oil but also its microscopic configuration (i.e., size, shape, orientation of the crystallites, and their aggregation state). The shift observed with an increase in $\dot{\gamma}_{max}$ indicates that there is an appreciable effect on such microstructural parameters due to the previous deformation history the material has experienced.

III. CRYSTALLIZATION AND WAXY CRUDE OILS MICROSTRUCTURE

The experimental results we have presented so far suggest that in order to understand the rheology of WCOs, we need to focus our attention on the underlying microstructure of the precipitated wax [39,60,79]. The main physical process that occurs in any WCO upon cooling is *crystallization* [36,37], and the secondary phase or the microstructure that arises from such a process is a network of agglomerated *wax crystals*. Figure 4 presents a schematic of the process and corresponding birefringence pictures of the model oil. The images were taken using an ABRIO (CRi, Inc.) camera and software on a Nikon TE-2000U inverted microscope using a $40\times$ objective. A small visualization chamber was made by applying three stripes (approximately $3 \times 20 \text{ mm}$) of parafilm on a glass slide ($75 \times 25 \text{ mm}$). The slide was then positioned on a hot plate at about 80°C and a cover glass ($22 \times 22 \text{ mm}$) was placed on top of the parafilm. Within a few seconds, the parafilm becomes transparent and the glass slide and cover are sealed, ready to be used for visualization. The oil/paraffin mixture was pipetted below the cover glass at the same temperature (80°C) and the slide was quickly placed under the microscope so that images could be recorded during the cooling process. Calibration of the ABRIO image processing software was performed by acquiring a background picture before filling the chamber with the mixture. Temperature was monitored with a type-K thermocouple mounted directly to the surface of the glass slide. Because of the low thermal conductivity of both glass and wax, we expect to have a difference of a few degrees between the actual temperature of the waxy oil sample and the temperature of the slide, and therefore in Fig. 4, we provide only an approximate value relative to the WAT.

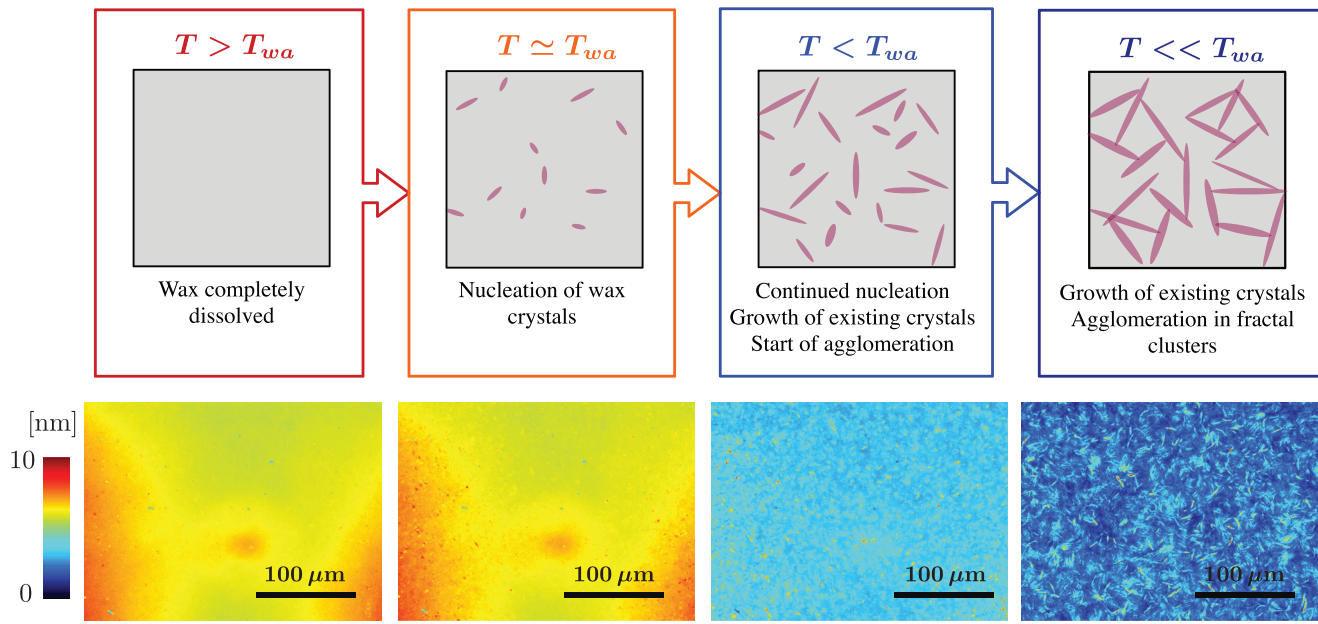


FIG. 4. Schematic diagrams and corresponding birefringence microscopy pictures of the wax nucleation and growth process in the same sample used for rheological measurements (10 wt. % paraffin wax in heavy mineral oil).

Figure 4 shows that for temperatures above the WAT, all the wax is fully dissolved in the oil; the sample is a transparent liquid with no evident microstructure and its behavior is Newtonian with Arrhenius dependence on temperature (cf. Fig. 2). As the WAT is approached, a few crystals have already nucleated and are enough to change the macroscopic behavior of the oil. As the temperature is lowered to values below the WAT, nucleation continues along with growth of the existing crystals. When the individual crystallites begin to approach each other, van der Waals forces come into play and they begin to form larger aggregates. The size and orientation of these aggregates are responsible for the rheological behavior we observe macroscopically. Several studies have focused on the morphology of single wax crystals [36,37,80], and we do not attempt to address the matter in detail here. The key feature is that the paraffin wax crystallizes primarily into discotic platelets [37,38,81], which can be regarded as strongly anisotropic solid objects. The lateral dimension of the platelets is a function of the temperature gradient under which they are formed but is typically on the order of $1 - 10 \mu\text{m}$ [38,40,82].

In order to understand the thermal and kinematic memory observed in the rheology of WCOs, there are two fundamental points to be addressed. First, the crystallization process has to be quantified so that at each given temperature the amount of wax that has precipitated out of solution is known. Second, the microscopic structure formed by the wax crystals has to be connected to the macroscopic behavior observed through rheological measurements. Other researchers have pointed out in the past that in order to understand the rheology of WCO, it is essential to understand the configuration of wax crystals [40,52,65,82]. However, so far the different experimental and theoretical approaches have had little success in finding a unified framework that can explain or model the rheological behavior of a WCO, with most methods being

limited to very specific sets of data and simple scaling laws [39,53,60].

An effective way to experimentally quantify the *amount* of precipitated wax is by using differential scanning calorimetry (DSC) [83–85], a simple and reliable thermoanalytical method that is widely used to study phase transitions [86–88]. In Secs. IIIA and IIIB, we describe the protocol used and the way the resulting cooling curves can be processed in order to eventually obtain the mass fraction of solid wax crystals. Identifying how to connect the microstructure to macroscopic quantities is, on the other hand, a more complex matter to address experimentally. Ideally, one should visualize and quantify the dynamics of a statistically significant number of wax crystals under the same shearing conditions that are realized in a rheometer [89], which is an extremely challenging task especially considering the wide variety of shear rates and temperatures that are typically experienced. In Sec. IV, we show how we can make progress using existing theories without the direct aid of observations of crystal orientation and interactions. To justify our assumptions, we will then test such arguments against experimental results and finally show how they can be incorporated into a full constitutive framework for TEVP materials such as WCOs.

A. DSC protocol and experimental results

DSC is a very well established technique, commonly employed to measure thermal properties of materials as well as study phase transitions [88,90]. Using a heat-flux type calorimeter [91] (Q100 DSC, TA instrument), about 6 mg of sample were placed in a pan, hermetically sealed by a manual press, and placed on one of the thermoelectric disks inside the instrument furnace. A second empty pan in the same furnace is used as a reference and the chamber was continuously purged with nitrogen. The instrument records

the differential heat flux (\dot{Q}) due to the temperature difference established between the reference pan and the sample pan [see top left of Fig. 5(a) for a simple schematic].

The two approaches most commonly used to study crystallization are based on investigating phase transitions either under isothermal conditions or under cooling/heating conditions [88]. We focus here on the process most relevant to the rheometric measurements, i.e., crystallization under cooling. We established a simple protocol to measure the heat flux during decreasing temperature ramps at different cooling rates (\dot{T}). The steps performed at each rate were the following: Equilibration of the sample at 60 °C for 5 min imposed temperature ramp at \dot{T} until the furnace temperature reaches -10 °C, and finally an increasing temperature ramp at a rate of 20 °C/min to heat the sample back to 60 °C. The results are shown in Fig. 5(a) for $\dot{T} = -2, -1.5$, and $-1\text{ }^{\circ}\text{C}/\text{min}$. Wax crystallization is a reversible thermodynamic process, and therefore, when the model waxy oil contains only paraffin, it can be cooled and heated multiple times without changing the nature of the material. This is why thermal beneficiation is useful as a way to erase any previous shear or thermal history in model waxy oils. In view of such reversibility and since, over the range of temperatures experimentally accessed, there is a very low chance of mass loss due to

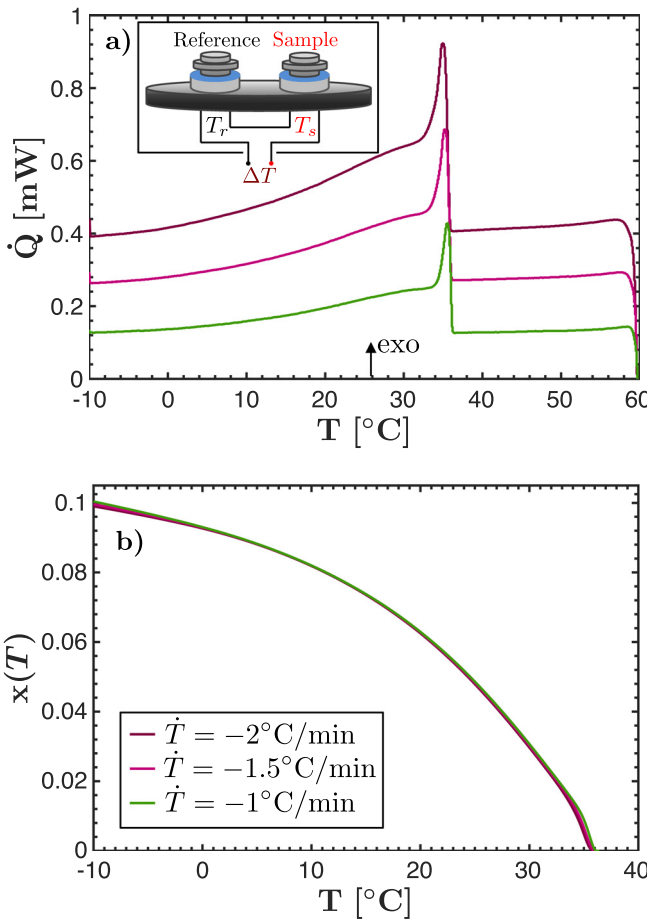


FIG. 5. (a) Thermal signature of the model oil obtained by DSC through cooling ramps at different cooling rates [$\dot{T} = -2, -1.5$, and $-1\text{ }^{\circ}\text{C}/\text{min}$, legend as in (b)]. On the top left: Schematic of a heat-flux differential scanning calorimeter; (b) mass fraction of wax obtained by integration of the raw data as described in Sec. III B.

evaporation, we performed all the DSC measurements sequentially on the same sample. This cannot be done on a real crude oil because other components may be present whose precipitation is not reversible, as well as light ends which tend to evaporate more easily [45,92].

Figure 5(a) shows the thermal response during the intermediate step of cooling for the three different cooling rates investigated. The initial steep slope at $T \simeq 60\text{ }^{\circ}\text{C}$ is an artifact due to the transient system response between the end of the isothermal equilibration step and the beginning of the cooling step. The heat flux then stabilizes at a constant value as the temperature decreases until the sample starts to crystallize. DSC measurements provide a more sensitive probe of phase transitions than rheological measurements and therefore the crystallization temperature measured with this technique provides a closer measure of the true *thermodynamic* WAT. This is because DSC can detect variations in the heat flux required to cool the sample even when the amount of precipitated wax is not enough to produce a substantial increase in viscosity. For the same reason, in most real crude oils, the *thermodynamic* WAT can be a few degrees higher than the *rheological* WAT; however, for this specific model waxy oil with a narrow distribution of carbons, the difference between the two measures is less than $1\text{ }^{\circ}\text{C}$, so the WAT that we measure with both techniques and the given protocols is the same ($T_{wa} = 37\text{ }^{\circ}\text{C}$). When the sample reaches this temperature, crystallization begins and the heat flux increases sharply, passing through a maximum within a relatively small extent of undercooling. As the temperature is decreased further, the heat flux begins to decrease, although the signal is strongly asymmetric about the peak heat flux. From our direct observations as well as other literature [38,40,42,82], we can briefly describe the crystallization process as characterized by nucleation and growth under supersaturation conditions [42]. Both processes take place continuously until equilibrium is achieved at the final temperature [40] with the number density of crystals being a function of the cooling rate [82]. What we focus on, in Sec. III B, is linking the raw heat flux signal to the amount of wax that has solidified, i.e., computing the mass fraction of crystallized wax and therefore obtaining an estimate of the volume fraction $\phi(T)$ of solid wax crystals as a function of temperature.

B. Mass fraction and volume fraction of crystallized wax

A robust procedure to obtain the mass fraction of solidified material from DSC measurements has been developed and used for different materials [83]. It works both for crystallization from the melt and for crystallization from mixtures, which is the present case. It is based on the fact that in an *ideal* experiment the baseline of the heat flux signal, i.e., the constant value of \dot{Q} before and after crystallization, should be equal to zero and the area beneath the heat flux peak can be related to the specific *latent heat of crystallization* (h_c). It follows that when integrating only up to a certain T at which crystallization is not yet complete, the computed quantity is a measure of the (extensive) *enthalpy of*

crystallization of the sample $[H_c(T)]$ as obtained from a constant cooling rate experiment, i.e., the amount of heat released between T_{wa} and T is

$$H_c(T) = \int_{t_{wa}}^t \hat{Q}(t') dt' = \int_{T_{wa}}^T \frac{\dot{Q}(T')}{\dot{T}} dT', \quad (1)$$

where the first integral is computed over time, while the second integral is expressed in terms of temperature. The conversion is achieved through a change of variable based on the relationship between time and imposed temperature $T(t) = T_i + \dot{T}t$, with T_i being the initial temperature. Knowing the total mass of the sample m_{tot} , $H_c(T)$ and h_c , the mass fraction of wax as a function of temperature can be easily computed as follows

$$x(T) = \frac{m_w^p(T)}{m_{tot}} = \frac{H_c(T)}{h_c m_{tot}}, \quad (2)$$

where $m_w^p(T)$ is the mass of precipitated wax at that temperature.

In a real instrument, the baseline is never completely flat and usually varies with the cooling rate, as evident from Fig. 5(a). As a consequence, the first step in analyzing DSC data requires a correction of the raw signal by subtraction of the baseline. There are several ways to achieve this and it must be verified that the results do not change significantly with the procedure chosen (refer to [88] for more details). The method we have implemented to correct for the baseline is to fit a line of constant slope to the heat flux measurements above the WAT (discarding the experimental points close to the initial transient to avoid instrument artifacts), and then subtracting this linear trend from the raw signal. A test was carried out to check that the results were not significantly affected by the choice of fitting points. The corrected data were finally numerically integrated using the trapezoid rule and the computed mass fraction is shown in Fig. 5(b) for the three different cooling rates. As expected from the composition of the model oil, the maximum value reached at the end of the crystallization process is 10%.

As will become clearer in Sec. IV, from a rheological viewpoint it is more important to know the volume fraction $[\phi(T)]$ rather than the mass fraction of solid particles. However, once the latter is evaluated it is possible to estimate $\phi(T)$ by using known values for the density of the mineral oil, the liquid paraffin wax and the solid paraffin wax. Based on the data available, we assumed that the densities were constant with temperature and equal to $\rho_o = 0.862 \text{ g/ml}$ for the mineral oil (taken from the MSDS of the product), $\rho_w^p = 0.9 \text{ g/ml}$ for the solid paraffin wax and $\rho_w^l = 0.86 \text{ g/ml}$ for the liquid paraffin wax. It is important to remember that, as precipitation occurs, the amount of liquid wax in the mixture decreases so that the total wax content (in the solid state + liquid state) is always equal to the amount initially in solution (m_w^{tot}). Then, the *actual volume fraction* $\phi(T)$ is

$$\phi(T) = \frac{V_w^p(T)}{V_w^l(T) + V_o}, \quad (3)$$

where $V_w^p(T) = m_w^p(T)/\rho_w^p$ is the volume of precipitated wax, $V_w^l(T) = m_w^l(T)/\rho_w^l = (m_w^{tot} - m_w^p)/\rho_w^l$ is the volume of wax still in solution with the oil, and $V_o(T) = m_o/\rho_o$ is the (unchanging) volume of the mineral oil. Note that we use the adjective *actual* to specify that this is the volume fraction the solid wax would occupy if the crystals filled all the space available without any void, that is, if they were growing as a pure polycrystalline solid. We shall see in Sec. IV that because the crystals grow as anisotropic and interacting platelets (cf. the birefringence images on Fig. 4), this markedly underestimates the value of the *effective volume fraction* that defines the rheological behavior of the model waxy oil.

IV. PROPOSED CONSTITUTIVE FRAMEWORK FOR WCO

So far we have discussed the results from a specifically designed set of rheological protocols on the model WCO and argued that the measured response must be a result of the evolution of the internal microstructure composed of solid, platelet-like wax crystals. To proceed further, we now quantify the coupling between the microstructure and macroscopic quantities and concurrently determine the evolution of the microstructure in response to applied deformation or stress. Our aim is to develop a constitutive framework able to describe all the observed rheological features in terms of a thermodynamically consistent and frame-invariant model.

Based on the birefringence images in Fig. 4 we note that, from a rheological point of view, a WCO below the WAT is very similar to a suspension of attractive, anisotropic, non-Brownian solid particles. What distinguishes WCOs from a generic suspension of solid particles is that while suspensions are usually prepared with a fixed composition, i.e., the actual volume fraction depends only on the amount of solid initially dispersed in the liquid, for a crude oil ϕ is not established *a priori* but depends on the temperature, as we have demonstrated by DSC. Hence, there is a one-to-one correspondence between temperature and actual volume fraction, such that we can specify one or the other. Since we have investigated the transient and steady shear rheology over a wide range of temperatures, our results are equivalent to the study of a corresponding number of oil/wax mixtures with varying wax contents. Although the amount of paraffin in solution does marginally affect the magnitude of the Newtonian viscosity of the liquid phase, it is the amount of precipitated wax that has a dominant role in determining the rheological behavior of the oil below the WAT. It is also important to note that the one-to-one correspondence between temperature and actual volume fraction resembles the very well established concept of time-temperature superposition in polymer physics [93]. It is therefore reasonable to assume that for WCOs there exists a *volume fraction-temperature superposition* which paves the way for an effective modeling approach for this class of TEVP materials as we show below.

A. Effective volume fraction and its kinematics

The mapping between volume fraction and temperature allows us to focus our attention on the analogies between

WCOs and suspensions. To understand how to couple the crystalline microstructure to macroscopic rheological properties, we draw on the extensive literature of solid suspensions. Much work has been done on this topic since the pioneering paper on dilute systems by Einstein [94], with many contributions first to the understanding of the dilute and concentrated regime with purely hydrodynamic interactions [95–97] and then the development of theories to describe the case of concentrated systems of interacting particles [98–100]. As noted previously, WCOs can be regarded as concentrated attractive suspensions of anisotropic wax crystals, composed primarily of thin platelets as schematically shown in Fig. 6, which are governed by both hydrodynamic interactions and interparticle forces.

1. Review of the model for attractive suspensions

We focus our attention on the theory introduced for the viscosity of aggregated suspensions by Snabre and Mills [54,101]. Their microrheological model is based on three main assumptions. First, in a concentrated system (without attractive forces), it is possible to account for the many-body hydrodynamic interactions by using a mean field theory based on estimation of the viscous dissipation in a fluid volume [101], which leads to the following expression for the relative viscosity of the suspension

$$\eta_r(\phi, \phi_{max}) = \frac{\eta(\phi, \phi_{max})}{\eta_0} = \frac{1 - \phi}{(1 - \phi/\phi_{max})^2}, \quad (4)$$

where η_0 is the Newtonian viscosity of the suspending fluid, ϕ is what we identified earlier as the actual volume fraction, and ϕ_{max} is the maximum packing fraction, i.e., the volume fraction above which the system is no longer fluidized ($\eta \rightarrow \infty$). In general, ϕ_{max} can be a function of the shear rate, especially for high shear rates and concentrations close to the maximum packing fraction [54,102]; however, for simplicity, we will take ϕ_{max} to be constant.

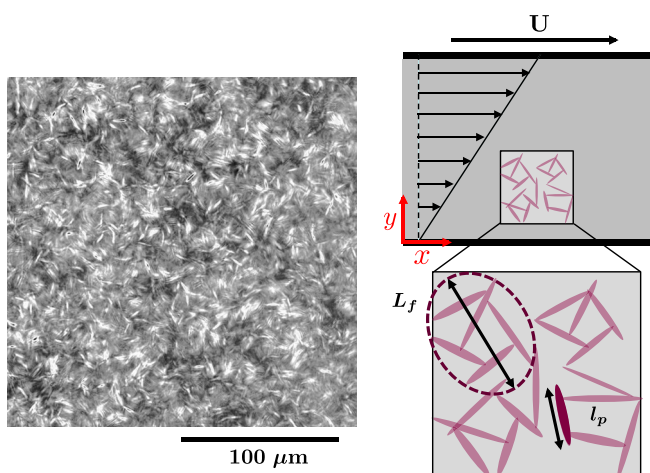


FIG. 6. Schematic of the model waxy oil under shear (right side) with characteristic dimensions of the wax crystals (l_p) and crystal agglomerates (L_f) used in the theory for flocculated attractive suspensions by Snabre and Mills [54,94]. Also shown (left side) is an actual birefringence image from an optical microscope using cross polarizers.

Snabre and Mills also consider the solid attractive particles to form fractal aggregates (cf. Fig. 6) with characteristic dimension (L_f) that is connected to the characteristic dimension of the elementary particle (l_p) and the number of particles in each cluster (N) by [54]

$$\frac{L_f}{l_p} \sim N^{1/D_f}, \quad (5)$$

D_f being the fractal dimension or Hausdorff–Besicovitch dimension [103] (see Appendix B). Lastly, in the microrheological model of Snabre and Mills, the fractal clusters are considered to be nonfreely draining and hence they are regarded hydrodynamically as spheres of radius L_f . As a consequence, the effective viscosity of the suspension (denoted η_e) can be found by equating the global apparent rate of viscous dissipation to the viscous dissipation rate that arises in the interstitial fluid between aggregates. Introducing an *effective volume fraction* defined as

$$\phi_e(T) = \phi(T) \left[\frac{L_f}{l_p} \right]^{(3-D_f)}, \quad (6)$$

the relative viscosity of a suspension of fractal aggregates can therefore be expressed as

$$\eta_r(\phi_e, \phi_{max}) = \frac{\eta(\phi_e, \phi_{max})}{\eta_0} = \frac{1 - \phi_e}{(1 - \phi_e/\phi_{max})^2}. \quad (7)$$

It is important to specify that this is effectively a *plastic viscosity*, since a percolated suspension of attractive particles is also expected to result in a certain yield stress τ_0 (itself a function of the actual volume fraction) below which there is no appreciable viscous flow. In the original work, the equation for the plastic viscosity [Eq. (7)] is used to compute the stress on the material when $\tau > \tau_0$ by assuming that the aggregates behave as if they were isolated from each other and surrounded by a medium of viscosity $\eta_e(\phi_e, \phi_{max})$, so that the stress they experience is simply $\tau = \eta_e(\phi_e, \phi_{max})\dot{\gamma}$. The theory also assumes that the cluster dimension L_f evolves as a function of the imposed shear stress through a specified algebraic equation. By combining these expressions, Snabre and Mills arrive at a nonlinear constitutive equation in τ that resembles the Casson model and that can be solved to obtain the shear viscosity at different shear stresses or shear rates.

Although this microrheological model has been successfully used in capturing the shear viscosity of certain types of suspensions, including that of some crude oils with modifications introduced by Palermo and Tournis [53], it has several limitations. In particular, (i) it does not allow the study of transient responses, as all the equations are algebraic and therefore designed only to capture steady state behavior; (ii) it does not consider the viscoelastic nature of the oil below the yield stress nor the complex yielding behavior close to the critical flow stress [56], and (iii) it cannot be easily extended to a three-dimensional, frame-invariant, and thermodynamically consistent constitutive theory. Consequently,

it is not suitable for predicting the mechanical response of WCOs in a computational flow assurance setting. However, its ability to describe the evolution in the plastic viscosity as a function of the effective volume fraction does capture the viscometric responses observed experimentally. In the next paragraph, we first focus our attention on this particular aspect.

2. Effectiveness of the fractal description: Capturing temperature effects

To test the ability of this fractal aggregate theory to describe the plastic viscosity of waxy oils, we consider the experiments described in Sec. II B 1 concerning the effect of temperature on the flow curves, measured by applying the experimental protocol introduced in Sec. II A. As we have noted, a decrease in the temperature leads to an increase in the plastic viscosity; however, the overall shape of the flow curves does not change leaving the underlying trend of the stress/strain rate relationship basically unaltered. Based on the knowledge of wax precipitation and its relationship with temperature, we can now explain these results by recognizing that the increase in the plastic viscosity is related to an analogous increase in the actual volume fraction of precipitated wax. If we assume that the functional relationship between $\phi(T)$ and $\eta(T)$ follows the mean field theory presented above, than we can say that

$$\eta_r(T) = \frac{\eta(\phi(T))}{\eta(\phi(T_{wa}))} = \frac{1 - \phi(T)\mathcal{F}(l_p, L_f, D_f)}{\left(1 - \frac{\phi(T)\mathcal{F}(l_p, L_f, D_f)}{\phi_{max}}\right)^2}, \quad (8)$$

where we have already substituted for Eq. (6) instead of using the effective viscosity and introduced, for convenience, a function \mathcal{F} that we call the *fractal connectivity*, defined as

$$\mathcal{F}(l_p, L_f, D_f) = \left[\frac{L_f}{l_p} \right]^{(3-D_f)}. \quad (9)$$

The fractal connectivity is a function that captures, in a coarse-grained sense, the morphology of the network generated by the wax crystals and carries information regarding the level of structuring occurring in the material. If $\mathcal{F} = 1$, then the aggregates contain only one crystal and the material is completely unstructured on larger scales. For values bigger than unity, the dimension of the clusters increases, meaning that each aggregate is formed from a finite number of crystals. Based on Eq. (8), we can see that the theoretical maximum of the fractal connectivity depends on the volume fraction $\phi(T)$ as $\mathcal{F}_{max} = \phi_{max}/\phi(T)$ at which point the material completely solidifies ($\eta \rightarrow \infty$); however, there is no evidence at the moment that even when the microstructure is left completely unperturbed the clusters will reach this equilibrium value \mathcal{F}_{max} . Finally, in Eq. (8) we have identified the Newtonian viscosity of the oil phase as the viscosity of the oil/paraffin wax mixture when $T = T_{wa}$. From the temperature ramp in Fig. 2(b), we can see that the WAT is the lowest

temperature that can still be fitted by the Arrhenius relationship before the wax precipitates, and hence, we pick this value as a measure of the viscosity at zero precipitated volume fraction, similarly to Visintin *et al.* [52].

In theory, all the variables that appear in Eq. (8) can be measured. The actual volume fraction is determined from DSC measurements as explained in Sec. III. The magnitude of the fractal connectivity can be evaluated by imaging the microstructure under flow and using box-counting methods to represent the power-law relationship between the cluster size and wax crystal. However, from a practical point of view, this is a rather complex task since it would require imaging the sample under shear with the same conditions realized in the rheometer. Although direct optical access into several geometries is possible, the partial opacity of the material itself and the necessity of roughening the surfaces to avoid slip make the task quite arduous. In the following, we therefore consider \mathcal{F} as a fitting parameter. Another variable that we will treat as a fitting parameter is the maximum packing fraction. Although in many studies ϕ_{max} is assumed to be equal to the value for spheres, there is evidence that in reality this quantity is strongly affected by the geometry of the particles [104], changing from 0.64 for spheres to 0.44 for rough crystals to 0.22 for elongated fibers with a large aspect ratio (i.e., strongly anisotropic objects) [104]. Trying to measure this value directly through rheometry can be challenging because as the maximum concentration is approached, wall slip occurs even on rough surfaces leading to large uncertainties on the actual value. As a consequence, we will treat ϕ_{max} as a fitting parameter with an expected range of $0.2 \leq \phi_{max} \leq 0.7$ according to Genovese [104]. This range is compatible with the results presented by Mathew *et al.* [105] who have looked at the connectivity percolation in a suspension of hard platelets by means of Monte Carlo simulations. In their work, the authors show that for hard cut spheres with various aspect ratios and interacting only through excluded volume interactions, the percolation threshold is below a volume fraction of 0.4.

Since we want to test the effectiveness of Eq. (8) exclusively, we need to calculate the relative plastic viscosity from the experimental data. The viscometric data in Fig. 2(b) show that above 100 s^{-1} the viscosity is approximately constant; therefore, we take the values of η measured at the maximum shear rate ($\dot{\gamma}_{max} = 500 \text{ s}^{-1}$) for all the temperatures investigated and divide these values by the value of the viscosity at the WAT that we read from the temperature ramp [cf. Fig. 2(a)]. By plotting this experimentally determined ratio as a function of the actual volume fraction $\phi(T)$, we can compare it directly to the expression for the theoretical plastic viscosity [Eq. (8)] with just two fitting parameters: The fractal connectivity \mathcal{F} and maximum packing fraction ϕ_{max} . The comparison is plotted below [see Fig. 7(b)] for a specific set of parameters and shows a very good agreement between experiments and theory.

Nevertheless, it could be argued that there are multiple sets of values which are still within reasonable physical limits and that can provide a comparably good agreement. In order to address this concern, we show that these fitting parameters allow us to obtain a master curve which

superposes all the flow curves above the dynamic yield stress at different temperatures based on shifting factors that depend, in this case, on the volume fraction. Based on estimates of the viscous dissipation in a fluid element from which Eq. (7) is derived, it can be easily shown that the *global* shear rate $\dot{\gamma}$ is related to the *local* shear rate $\dot{\gamma}_r$ through the relationship [54]

$$\dot{\gamma}_r = \frac{\dot{\gamma}}{\left(1 - \frac{\phi_e}{\phi_{max}}\right)} = \frac{\dot{\gamma}}{\left(1 - \frac{\phi \mathcal{F}}{\phi_{max}}\right)}, \quad (10)$$

where $\phi_e = \phi \mathcal{F}$ is the effective volume fraction of the solid fractal aggregates. Consequently, from Eq. (8), we can deduce that the local stress should scale as

$$\sigma_r = \frac{\sigma(1 - \phi_e)}{\left(1 - \frac{\phi_e}{\phi_{max}}\right)} = \frac{\sigma(1 - \phi \mathcal{F})}{\left(1 - \frac{\phi \mathcal{F}}{\phi_{max}}\right)}. \quad (11)$$

If we plot all the different experimentally measured flow curves in terms of these rescaled variables as shown in Fig. 7(a), we observe that for one specific set of parameters ($\mathcal{F} = 2.2$, and $\phi_{max} = 0.28$) all of the flow curves superpose with good agreement over the entire region of plastic flow, from the shear rate corresponding to the dynamic yield stress up to $\dot{\gamma}_{max}$.

This superposition means that the values of the dynamic yield stress in the WCO as a function of the actual volume fraction of wax will also follow the same trend as the plastic viscosity. This is surprising because in most of the literature on attractive suspensions [102,106], including the work of Snabre and Mills [54,101], the yield stress usually follows a different trend (although there is not a universal agreement on one specific functional form). In general, however, the functional forms proposed in the literature do not predict a significant yield stress below 10% by volume of suspended particles. By contrast, from the experiments we can clearly see that for this model waxy oil even wax contents as low as 2% are sufficient to generate a measurable yield stress, suggesting strongly attractive and highly fractal objects. It is clear from Fig. 7(c) that this functional form adequately describes the evolution in σ_{dy} above 2% wax content, while in the region $\phi \leq 0.02$ (or temperatures $32^\circ\text{C} \leq T \leq T_{wa}$), where the amount of precipitated wax is right at the edge of the value known as the gelation volume fraction [54], we can expect that a transitional regime can apply. It is important to note that while the plot of the relative viscosity can be normalized to unity, for the yield stress we cannot do the same because at zero volume fraction there is no yield stress in the system (it is a Newtonian oil). Therefore, from the form of Eq. (8) we note that for $\phi \geq 0.02$ the following expression for the yield stress holds

$$\sigma_{dy}(T) = \sigma_{dy}^0 \frac{1 - \phi(T)\mathcal{F}}{\left(1 - \frac{\phi(T)\mathcal{F}}{\phi_{max}}\right)^2}, \quad \phi \geq 0.02, \quad (12)$$

and we determine that $\sigma_{dy}^0 = 0.31 \text{ Pa}$ from fitting.

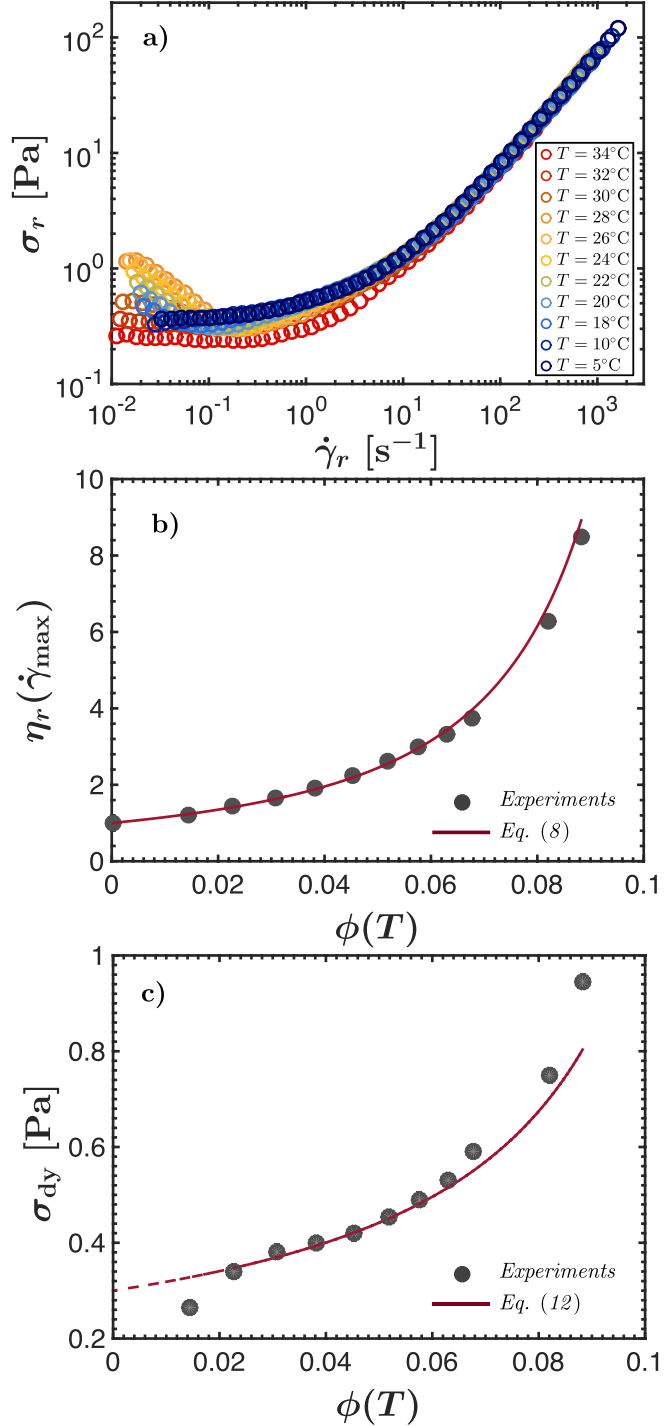


FIG. 7. (a) Master curve generated by rescaling the shear rate and shear stress based on Eqs. (10) and (11) (see text); (b) evolution in the relative viscosity with crystallite volume fraction (symbols) computed at the highest shear rate ($\dot{\gamma} = 500 \text{ s}^{-1}$) and theory (solid line); (c) dynamic yield stress σ_{dy} (symbols) and value predicted by the theory (solid line) with $\sigma_{dy}^0 = 0.31 \text{ Pa}$.

Finally, we emphasize that, as discussed in Sec. II B 1, at very low shear rates when the stress falls below the dynamic yield stress, steady viscometric flow may not necessarily be sustainable in the sample and therefore we do not expect the measured data to follow the simple proposed scaling as measurements can be affected by shear banding instabilities and slip [56,66,67]. However, the ability of the fractal aggregate model for plastic viscosity to capture the thermal

sensitivity of these fluids provides confirmation that the effects of temperature observed in the present work and in previous studies [40,53,55,56] can be explained by recognizing that WCOs below the WAT are fractal suspensions of wax crystal aggregates. In addition, the fact that rheological master curves can be constructed with just one set of two fitting parameters (\mathcal{F} , ϕ_{max}) substantiates the observation that the microstructural evolution is similar at all temperatures below the WAT, and what changes is the material composition, i.e., the actual volume fraction $\phi(T)$ of precipitated wax.

3. The kinetics of fractal aggregates and thixotropy

In order to model flow assurance problems encountered with thixotropic materials such as WCOs, it is important to understand the kinetics of aggregation which can also describe transient responses such as the evolution of the stress during the shear rejuvenation step. To do so, we proceed based on a continuum approach that has been proposed and used in many works to account for thixotropy [8,15], even in the context of WCOs [56] although not specifically for the plastic viscosity. The approach is that of introducing a single *structural parameter* (denoted generically λ) which provides a scalar measure of the microstructure and that usually varies between $\lambda=0$, to represent a fully unstructured material, and $\lambda=1$, for a completely percolated network. In the theory for fractal aggregates, we have already introduced a scalar measure of the microstructure, i.e., the fractal connectivity $\mathcal{F}(\dot{\gamma}, t)$, which at this point we can clearly state is a function of shear rate and time. However, we have already seen that its values are not limited to the same bounds (the interval $[0, 1]$). In order to construct a suitable measure, we therefore normalize $\mathcal{F}(\dot{\gamma}, t)$ and introduce the following structural parameter $\xi(\dot{\gamma}, t)$:

$$\xi(\dot{\gamma}, t) = 1 - \frac{1}{\mathcal{F}(\dot{\gamma}, t)}, \quad (13)$$

henceforth referred to as *normalized fractal connectivity*. We deliberately choose not to identify this measure with the symbol λ for reasons that will become clear in Sec. IV B.

The normalized fractal connectivity is now a scalar structural parameter that varies between zero and one assuming that, as a limit, $\mathcal{F} \rightarrow \infty$ for a completely percolated structure. With this change of variables, we are able to write down an evolution equation for the structural parameter and we choose to write it in the form first introduced by Moore [107] based on pioneering work by Goodeve and Whitfield [108]

$$\dot{\xi} = \frac{1}{\tau_{th,v}} (\xi^* - \xi) - \beta_v \xi |\dot{\gamma}^p|^n, \quad (14)$$

where the “over-dot” notation is used for the time derivative. This expression is an evolution equation relating the steady state value of the normalized fractal connectivity to the equilibrium established, at each given shear rate, between the

interparticle attractive forces that tend to build up fractal aggregates (first term on the RHS) and the viscous forces that develop as a result of the plastic shear rate that tend to break down the clusters into smaller entities (second term on the RHS). The time scale over which structural build up occurs is denoted as $\tau_{th,v}$ and it is effectively a thixotropic time scale for the viscous behavior. The break down conversely is proportional, through an unknown parameter β_v , to the plastic shear rate via a power law dependence. Because the fractal connectivity \mathcal{F} never practically reaches infinity, the maximum value that ξ can assume under static conditions (i.e., with no plastic deformation) is smaller than unity and we indicate it generically by ξ^* .

Compared to other commonly used evolution equations there are two main differences. First of all, we assume that only plastic deformations can actively change the level of structuring, meaning that if we perturb the material in the viscoelastic regime we do not expect any effect on the microstructure, while if we strongly deform the waxy oil into the plastic region the effect should depend on the magnitude but be independent of the direction in which we are applying the shear. This is a reasonable assumption that has been successfully used before even in the context of WCOs [56] and it is consistent with the idea that a certain stress threshold has to be overcome to break the crystals apart. Second, in order to account for the fact that ξ can never exactly be equal to one (corresponding to infinite fractal connectivity \mathcal{F}), we write the driving force for build up of fractal aggregates not proportional to $(1 - \xi)$ but to $(\xi^* - \xi)$. Based on the discussion for the fractal connectivity and its theoretical maximum value $\mathcal{F}_{max}(\phi(T))$, we can deduce that the theoretical maximum value for the normalized fractal connectivity should be $\xi_{max}(\phi(T)) = 1 - \phi(T)/\phi_{max}$ and thus as a first approximation we can assume $\xi^* = \xi_{max}$ (we leave further discussion on this subject to Appendix D). For now, we simply remark that one advantage of this assumption is that it reduces the number of unknown parameters that need to be fitted since it is based on a measurable quantity ($\phi(T)$) and a previously determined model parameter (ϕ_{max}). It is worth noticing that, from a mathematical point of view, a change of variable could be performed by rescaling ξ with ξ^* and obtaining a truly normalized quantity. This way Eq. (14) would be equivalent in form to those already introduced in the literature for the evolution in plastic viscosity. However, from a physical perspective, it is very important to recognize the meaning and the limits associated with the normalized fractal connectivity. In the reminder of the paper, ξ and Eq. (14) are preferred and used, but we emphasize here that no substantial change to the model presented would be necessary if a rescaling of this microstructural variable were to be implemented.

Lastly, we want to point out that, for certain materials, the evolution equation for the structural parameter could also include an additional term that takes into account the possibility of shear induced flocculation, that is, there should be an additional term proportional to $|\dot{\gamma}^p|$ that positively contributes to a change in ξ . We do not include such a term because in most of our experiments we find that the importance of this phenomenon is limited compared to the two other

mechanisms, and in the principle of parsimony we consciously omit the extra term. However, an extension of Eq. (14) to include such a shear-induced structuration is extremely straightforward and can be done at any point without changing fundamentally the framework here proposed. Similarly, we do not include at this stage any effect due to temperature gradients. Based on experimental observations [82], it is expected that the effective volume fraction be a function of the cooling rate; however, a set of definitive experimental results that would allow us to determine how ϕ_e and therefore ξ depend on \dot{T} has not been performed yet and we reserve such endeavor for a future work.

Based on the definition of the normalized fractal connectivity [Eq. (13)], we can now rewrite the plastic viscosity in terms of ξ (or if preferred ξ/ξ^*) to explicitly show that we have a dependence not only on temperature but also on the plastic shear rate and time

$$\eta_r(T, |\dot{\gamma}^p|, t) = \frac{\eta(\phi(T))}{\eta(\phi(T_{wa}))} = \frac{1 - \frac{\phi(T)}{1 - \xi(|\dot{\gamma}^p|, t)}}{\left(1 - \frac{\phi(T)}{\phi_{max}} \frac{1}{1 - \xi(|\dot{\gamma}^p|, t)}\right)^2}. \quad (15)$$

Equations (14) and (15) now provide us with a mechanism to explore if the evolution equation for the normalized fractal connectivity captures our experimental results. If we reconsider Fig. 3(a), we now have an expression to compute such curves theoretically and use the comparison as a fitting to determine the parameters $\tau_{th,v}$, β_v , and n . To this end, we notice that Eq. (14) has an analytical solution for a constant imposed shear rate, as we can assume that, for the parameter values investigated, the contribution from viscoelasticity yields a shear rate that is negligible compared to the plastic shear rate, so we can approximate $\dot{\gamma} \simeq \dot{\gamma}^p$. The resulting first order ODE can be analytically solved to give

$$\xi(|\dot{\gamma}^p|, t) = (\xi_0 - \xi_{ss}) \exp\left(-\frac{\xi^* t}{\tau_{th} v \xi_{ss}}\right) + \xi_{ss}, \quad (16)$$

where ξ_0 and ξ_{ss} are, respectively, the values of the normalized fractal connectivity at the beginning of the beneficiation step and at steady state. The value at steady state can be easily computed from Eq. (14) by setting $\dot{\xi} = 0$, which gives

$$\xi_{ss} = \frac{\xi^*}{1 + \beta_v \tau_{th,v} |\dot{\gamma}^P|^n}. \quad (17)$$

By using Eqs. (16) and (17) in Eq. (15), we can compare the predictions for the evolution in stress during shear rejuvenation with our experimental measurements to see how well a unique set of fitting parameters can capture the trends observed at different shear rates. To do so, we take the correct value of the volume fraction from the DSC measurement [$\phi(T = 26^\circ\text{C}) = 0.043$], we fix the maximum packing fraction to the same value that has been determined from the data at different temperatures ($\phi_{max} = 0.28$) and we

determine ξ_0 , $\tau_{th,v}$, β_v , and n through a fitting procedure. We use a numerical algorithm in MATLAB[®] that takes the data from the highest shear rate, fits one curve using a nonlinear least square regression method, and then updates the initial conditions before moving to the next data set. Lower and upper bounds on the fitting parameters are provided to ensure that the results are physically meaningful and iterations are monitored for each data set until a single set of model parameters is obtained that describes all the data with minimum standard deviation between the model and the measured data.

Figure 8(a) shows the results of this model fitting against the experimental data for all the different shear rates. The

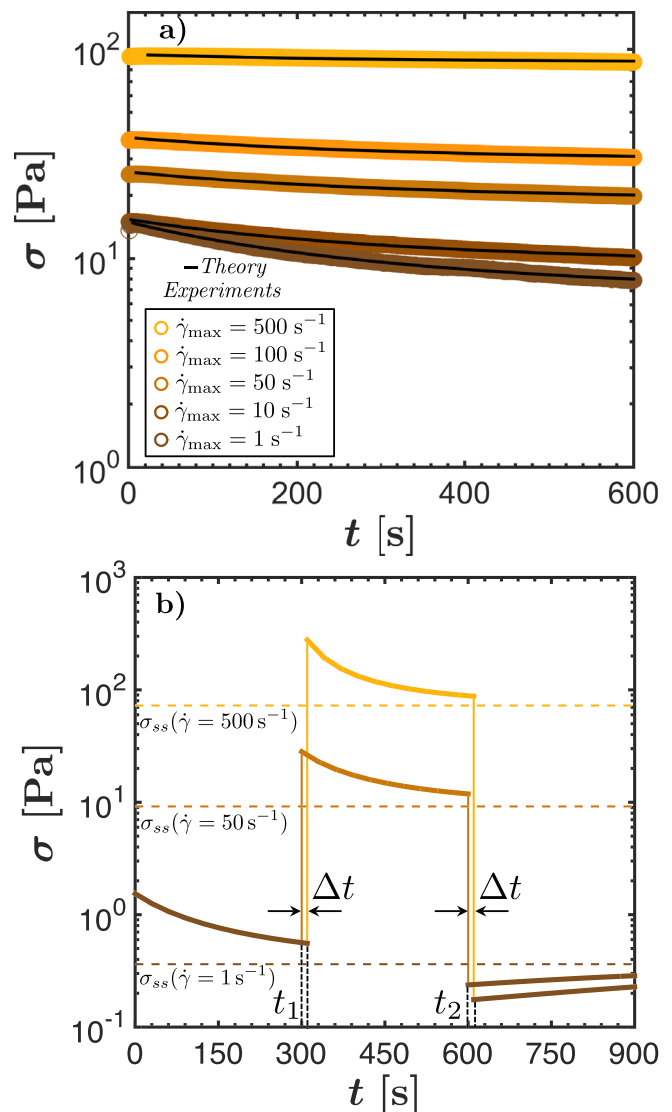


FIG. 8. (a) Comparison of experimental data from Fig. 3(a) on the time evolution of the stress observed during the beneficiation step at different shear rates ($\dot{\gamma}_{max}$). The black solid lines show model predictions obtained by setting $\tau_{th,v} = 460$ s, $\beta_v = 3.2 \times 10^{-4}$ s $^{1-n}$, and $n = 0.24$; (b) predictions of shear rate step changes (solid lines) based on Eqs. (16), (17), and (15) with values of the parameters as derived from part (a). Dashed lines represent the steady state value at the indicated shear rate [colors match with the legend in part (a)]. Two cases are presented, both of them starting from steady shear at $\dot{\gamma} = 1$ s $^{-1}$. In one case after $t_1 = 300$ s the shear rate is increased to $\dot{\gamma} = 50$ s $^{-1}$ for $t_2 = 300$ s and then decreased again to $\dot{\gamma} = 1$ s $^{-1}$. In the second case, the intermediate shear rate is raised to $\dot{\gamma} = 500$ s $^{-1}$.

predictions from the analytical solution to the evolution equation for the normalized fractal connectivity substituted into the equation for the plastic viscosity [Eq. (15)] are marked with a solid black line and they are in extremely good agreement at any shear rate. The values of the fitting parameters that appear in the evolution equation for ξ are: $\tau_{th,v} = 460$ s, $\beta_v = 3.224 \times 10^{-4}$ s $^{n-1}$, and $n = 0.24$. This comparison shows that the fractal aggregate model predicts not only the temperature effect but also captures the thixotropic nature of the viscous response and allows us to understand why we observe a decrease in viscosity during steady shearing at a constant temperature and thus why the value of the viscosity reached at the end of the temperature ramps differs from the value measured in the flow curve. When the wax crystals solidify they undergo two different processes: One is the soft attraction due to van der Waals forces that tends to aggregate them, and the other one is the disruption of fractal aggregates due to the level of shearing. From the best fit values of the model parameters, we can see that the thixotropic time scale is actually very long, so that the decay in microstructure toward steady state is very slow. Interestingly, as observed in the experiments, the time scale required to reach steady state is inversely proportional to the shear rate and therefore it takes less time to reach steady state at higher shear rates.

In Fig. 8(b), the same analytical solution with fitted values of the parameters, as obtained from the shear rejuvenation curves, is used to predict the behavior in stepwise changes of the strain rate. Two different cases are presented (solid lines), both of them starting from steady shear flow at $\dot{\gamma} = 1$ s $^{-1}$. In the first case, after $t_1 = 300$ s, the shear rate is increased to $\dot{\gamma} = 50$ s $^{-1}$ for $t_2 = 300$ s before being decreased back to $\dot{\gamma} = 1$ s $^{-1}$. In the second case, the intermediate shear rate is raised to $\dot{\gamma} = 500$ s $^{-1}$ after $t = t_1 + \Delta t$ with $\Delta t = 10$ s, the shift being added simply to provide clarity for the reader. Dashed lines indicate the steady state values of the stress at each simulated shear rate. The trends of the stress as a function of time are very similar to what has been experimentally observed on different WCOs before [52,55]. From this numerical experiment, we can clearly see that the fractal aggregate model allows us to predict a plastic viscosity which strongly depends on the shear history. In fact, the initial value of the viscosity at any given shear rate depends on the deformation that the material has undergone previously and the time required to reach its theoretical steady state value varies accordingly. This holds both when increasing and when decreasing the shear rate, resulting in the overshoots and undershoots apparent in Fig. 8(b) immediately after a step change in shear rate. The *steady state* value of the viscosity at a given temperature is not affected by the shear history; therefore, the model predicts that when a constant shear rate is applied for a sufficiently long time ($t/\tau_{th,v} \gg 1$), the viscosity (and therefore the shear stress) should reach a constant value independent of the previous deformation. These results suggest that the irreversibility sometimes observed in experiments for the plastic viscosity (see for example [55] for a similar system) might be due to the fact that the time over which the experiment was carried out is smaller than the required time to reach true

equilibrium. A more definitive set of experiments on model and real WCOs should be designed in order for this question to be properly addressed.

B. Fractal IKH model

So far, we have addressed some of the unique features observed experimentally for the model waxy oil in a specific test protocol; however, we have yet to lay out a complete constitutive framework that can be used to address an arbitrary thermokinematic history. In the present section, we outline a one-dimensional version of a thermomechanical model for TEVP WCOs. A full three-dimensional, frame-invariant version based on the Kröner–Lee decomposition is also being developed and will soon be reported separately for use in more advanced numerical simulations. Here, we focus our attention on the structure of the model and its physical interpretation. To this end, we do not introduce the model by presenting the rigorous sequence of steps through which it has to be derived (following the Coleman–Noll procedure [109] and using the Principle of Virtual Power [59] as already shown in part elsewhere for the IKH model [56,110]). We do emphasize though that such procedures are commonly used in continuum mechanics to derive constitutive equations that are thermodynamically consistent and have been already applied to the IKH model. Although they differ from the formal approaches more commonly used for complex fluids, based on the principle of reciprocity introduced by Onsager [111,112] and further developed by Beris and Edwards [113] and Grmela and Öttinger [114,115], the procedures used to derive the IKH model do satisfy *both* laws of Thermodynamics, under *any* process, *irrespective* of the number and type of internal variables and do not hold only in an approximate fashion (see [113], p. 150).

The proposed framework integrates the isothermal IKH model [56] with the SoFAs theory [54] as presented in our modified form above, and we therefore refer to it as the *fractal IKH* (FIKH) model. As in the original IKH model, the FIKH model uses a number of internal variables, in addition to the known kinematic and dynamic quantities, to prescribe a set of constitutive equations. Four internal variables arise: A tensorial strain measure \mathbf{A} that accounts for the damage accumulated in the microstructure and that is used to capture the kinematic hardening (KH) process (also known as the Bauschinger effect, see [59,61,116] for more details, as well as Appendix C) plus three scalar variables. Because we present here a one-dimensional version, \mathbf{A} reduces to a scalar with an associated sign, equivalent to a strain measure. The first scalar variable, denoted λ , is a structural parameter used to account for the isotropic hardening (IH) process, i.e., the isotropic expansion or contraction of the yield surface associated with plastic deformations [56,59] (see Appendix C). The second one is also a structural parameter indicated by ξ and describes the evolution in the normalized fractal connectivity. Two different structural parameters are essential because it is evident from experiments that the time scale over which the yield surface evolves during deformation is significantly shorter than that associated with the evolution of the plastic viscosity in the flowing wax. The third internal

scalar variable is the actual volume fraction $\phi(T)$ which can be easily measured as shown in Sec. III and therefore does not need any additional fitting.

Because the primary focus of the work is flow assurance, we do not address in detail the rich viscoelastic behavior of the material below yield. We take the simplest Maxwell model for the linear viscoelastic region, coupled in series with a plastic element that accounts for both isotropic hardening and KH as shown schematically in Fig. 9. However, the FIKH framework can be easily extended to incorporate a more elaborate viscoelastic model below yield and has the potential to describe other types of TEVP materials. Note that by adding a specific functional form for our plastic element we clearly separate viscoelasticity from plasticity and thixotropy and therefore our model is indeed an example of a constitutive model for a nonideal thixotropic material [20].

a. Kinematics and dynamics. We start by stating the kinematic assumptions used to quantify the magnitude and the rate of deformation of the mechanical analog depicted in Fig. 9. Because we expect the elastic deformation to be much smaller than the plastic response, we can assume that the total deformation is given by a simple superposition

$$\gamma = \gamma^{ve} + \gamma^p = \gamma^e + \gamma^v + \gamma^p, \quad (18)$$

where the second equality is a consequence of the particular choice of the Maxwell viscoelastic model. For the same reason, we can write an equivalent relationship also for the strain rate

$$\dot{\gamma} = \dot{\gamma}^{ve} + \dot{\gamma}^p = \dot{\gamma}^e + \dot{\gamma}^v + \dot{\gamma}^p. \quad (19)$$

Note that there is no restriction in assigning a different response for the viscoelastic strain γ^{ve} below yield, either for WCOs or when applying this framework to a different TEVP material.

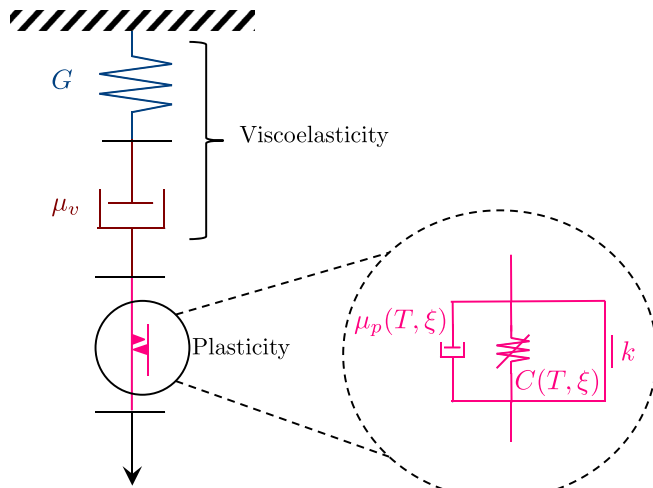


FIG. 9. Mechanical analog representing the FIKH model, composed of a Maxwell viscoelastic element in series with a plastic element that features both isotropic and KH processes. The fractal aggregate framework makes both the plastic viscosity μ_p and the back stress modulus C a function of temperature (T) and normalized fractal connectivity (ξ).

Since the elements are in series, we have a simple relation in 1D among the shear stresses acting on each element

$$\sigma = \sigma^{ve} = \sigma^p = \sigma^e = \sigma^v. \quad (20)$$

b. Constitutive and evolution equations. We begin with the simple form of the stress/strain relationship for the elastic solid which follows a classical Hookean model:

$$\sigma^e = G\gamma^e, \quad (21)$$

where G is the shear modulus (in Pa). Likewise, the stress/strain rate relationship for the viscous element of the Maxwell model follows a Newtonian liquid constitutive response:

$$\sigma^v = \mu_v \dot{\gamma}^p, \quad (22)$$

with μ_v the Newtonian viscosity (in Pa s). For simplicity, we consider both the shear modulus and the viscosity as constant material properties in this work, since their exact value does not affect significantly the response in steady shearing flow above yield. However, more detailed microstructural modeling below yield could capture additional dependencies on the fractal connectivity ξ and the volume fraction $\phi(T)$.

The most interesting and challenging step is to define the plastic flow rule. This relationship must capture all of the unique features we have observed earlier from the experiments. We start from the framework of the IKH model [56] and introduce the concept of an internal *back stress* (σ_{back}) to account for the presence of KH (or the Bauschinger effect, see for example [59] and references therein) in the microstructure and a *yield stress function* (σ_y) to account for IH. The back stress is effectively an internal stress that builds up because of the damage accumulated in the fluid microstructure [59,117]. It represents the energy stored in a reconfiguration of the microstructure due to inelastic deformations and has been extensively studied to describe hardening in metals [110,117,118]. Here, we build upon concepts introduced in the plasticity literature and further developed in the IKH model to adapt KH to WCOs (see [56,61] for further details as well as Appendix C). To this end, we recognize that the defects which give rise to such damage, or in other words, a reconfiguration of the internal arrangement of particle-particle bonds as well as aggregate-aggregate bonds compared to the equilibrium static morphology, can be created as well as destroyed by the applied deformation and therefore the back stress is written as a function of a strain measure A that evolves with the following equation [56,61]:

$$\dot{A} = \dot{\gamma}^p - (q|A|)^{\nu} \text{sign}(A)|\dot{\gamma}^p|. \quad (23)$$

Note that, because of the recovery term that depends on the material parameter q , the back stress does not increase indefinitely with the plastic strain but reaches a saturation level. The relationship between σ_{back} and A is assumed to be linear [56,61]

$$\sigma_{back}(T, \xi, A) = C(T, \xi)A, \quad (24)$$

where C is a back stress modulus (in Pa). The value of the back stress ultimately coincides with the value of the dynamic yield stress ($\sigma_{dy} \equiv \sigma_{back}$) [49], and in the original isothermal formulation it is taken as a material constant. However, we have already seen in Sec. IV A 2 that to account for temperature and shear rate effects through the idea of effective volume fraction, the back stress must depend on temperature and normalized fractal connectivity. Assuming that the evolution equation for the strain measure A is unchanged [Eq. (23)], we associate changes in the back stress with changes in the mechanical strength of the material microstructure represented by the back stress modulus C . Hence, the direct dependence of C on temperature and normalized fractal connectivity follows the expression previously introduced for σ_{dy} [cf. Eq. (12)], such that

$$C(T, \xi) = C_0 \frac{1 - \frac{\phi(T)}{1 - \xi}}{\left(1 - \frac{\phi(T)}{\phi_{max}} \frac{1}{1 - \xi}\right)^2}. \quad (25)$$

While the temperature is governed by the conservation of energy equation that should be solved locally with proper boundary conditions, the fractal connectivity is an additional variable which evolves according to Eq. (14).

For the yield stress σ_y we retain the formulation of the original IKH model. As introduced by Dimitriou and McKinley [56], we assume that the yield stress depends on the structural parameter λ through a simple linear relationship

$$\sigma_y(\lambda) = k\lambda, \quad (26)$$

where k is a modulus with units of Pa. The microstructural variable λ evolves through its own evolution equation that can be written as follows

$$\dot{\lambda} = \frac{1}{\tau_{th,y}} (1 - \lambda) - \beta_y \lambda |\dot{\gamma}^p|. \quad (27)$$

This equation, by analogy to the evolution equation for the normalized fractal connectivity, represents a balance between a gelation mechanism which produces a stronger microstructure (increasing the value of λ) and shear rejuvenation which decreases the strength of the crystal network

(decreasing λ). The time constant associated with the build up is indicated by $\tau_{th,y}$, while the coefficient of proportionality for the flow-induced destructuring is indicated by β_y . We emphasize once again that rheological measurements in the region between the dynamic yield stress (corresponding to the value of the back stress in steady flow $\sigma_{back} = C/q$) and the static yield stress (corresponding to σ_y) are subject to instabilities as discussed above, therefore we do not attempt to use bulk rheological data to identify specific trends as a function of temperature until further investigation of the stability of the flow field along this decreasing branch of the flow curve is performed. In theory though, it is possible to expect a dependence of k upon temperature and this can be implemented in the current framework at any point by specifying the functional form of $k = \hat{k}(T)$.

As observed above, λ and ξ have many features in common. They both represent a measure of the level of structuring within the material and they share similar evolution equations. However, the material constants associated with the two variables are extremely different: For our WCO we find $\tau_{th,y} = 10$ s while $\tau_{th,v} = 460$ s. Additional experiments or microstructural modeling are necessary to fully understand these dynamical processes; however, it is quite reasonable to expect that the time scale over which large aggregates evolve may be much longer than that over which an initial mechanically percolated network is established or destroyed upon shearing, principally because the length scales over which the corresponding microstructural rearrangements take place are very different, as recognized and suggested in two pioneering works published by Mewis over 40 years ago [119,120]. This is consistent with the concept of having thixo-viscous and thixo-plastic responses that do not necessarily coincide [20] and therefore do not evolve in the same way.

The introduction of an internal back stress and a yield stress function enables specification of a suitable plastic constitutive equation. First, we note that the plastic shear rate can be written as the product of its magnitude ($|\dot{\gamma}^p|$) and direction (\mathbf{N}^p)

$$\dot{\gamma}^p = |\dot{\gamma}^p| \mathbf{N}^p. \quad (28)$$

The magnitude of the shear rate is related to the stress by the following flow rule [56]:

$$|\dot{\gamma}^p| = \begin{cases} 0 & \text{if } |\sigma - \sigma_{back}(T, \xi, A)| \leq \sigma_y(\lambda) \\ \left(\frac{|\sigma - \sigma_{back}(T, \xi, A)| - \sigma_y(\lambda)}{\mu_p(T, \xi)} \right)^{1/m} & \text{if } |\sigma - \sigma_{back}(T, \xi, A)| > \sigma_y(\lambda), \end{cases} \quad (29)$$

where the *effective stress* ($\sigma_{eff} = \sigma - \sigma_{back}$) accounts for the fact that the stress absorbed by the deformation of the microstructure does not contribute to plastic flow. The

direction of the flow instead is given by the assumption of codirectionality [59,121] between stress and plastic strain rate, hence

$$N^p = \frac{\sigma_{\text{eff}}}{|\sigma_{\text{eff}}|} = \frac{\sigma - \sigma_{\text{back}}}{|\sigma - \sigma_{\text{back}}|}. \quad (30)$$

Equation (29) essentially states that whenever the effective stress exceeds the yield stress, which itself depends on the level of microstructural organization, the material flows with a pseudoplastic viscosity μ_p , the adjective pseudo coming from the fact that μ_p has units of Pa s^m .

In the original IKH model, the pseudoplastic viscosity was taken to be a constant material parameter; however, we have shown in Sec. IV A that if we account for the dependence of the plastic viscosity on the fractal network of wax crystals, we can capture both the effect of temperature on the material response and the viscous thixotropic behavior. Based on Eq. (15), in the FIKH model we therefore expect μ_p to have the following functional form of the temperature and normalized fractal connectivity

$$\mu_p(T, \xi) = \mu_p^0 \frac{1 - \frac{\phi(T)}{1 - \xi}}{\left(1 - \frac{\phi(T)}{\phi_{\max}} \frac{1}{1 - \xi}\right)^2}, \quad (31)$$

TABLE I. Summary of the important equations for the FIKH model and list of parameters. For a detailed description refer to the text (Sec. IV B).

Fractal IKH model	
	Kinematics
Strain decomposition	$\gamma = \gamma^{ve} + \gamma^p$ (18)
Strain rate decomposition	$\dot{\gamma} = \dot{\gamma}^{ve} + \dot{\gamma}^p$ (19)
Viscoelastic strain (Maxwell model)	$\gamma^{ve} = \gamma^e + \gamma^v$ (18)
	Dynamics
Mechanical stress balance	$\sigma = \sigma^{ve} = \sigma^p$ (20)
Viscoelastic stress (Maxwell model)	$\sigma^{ve} = \sigma^e = \sigma^v$ (20)
	Constitutive equations
Viscous element	$\sigma^v = \mu_v \dot{\gamma}^v$ (22)
Elastic element	$\sigma^e = G \gamma^e$ (21)
Plastic element	$\dot{\gamma}^p = \dot{\gamma}^p N^p$ (28)
Plastic shear rate magnitude	$ \dot{\gamma}^p = \begin{cases} 0 & \text{if } \sigma_{\text{eff}} \leq \sigma_y \\ \left(\frac{ \sigma_{\text{eff}} - \sigma_y}{\mu_p}\right)^{1/m} & \text{if } \sigma_{\text{eff}} > \sigma_y \end{cases}$ (29)
Plastic shear rate direction	$N^p = \frac{\sigma_{\text{eff}}}{ \sigma_{\text{eff}} } = \frac{\sigma - \sigma_{\text{back}}}{ \sigma - \sigma_{\text{back}} }$ (30)
Internal back stress	$\sigma_{\text{back}} = CA$ (24)
Yield surface	$\sigma_y = k\lambda$ (26)
Back stress modulus	$C = C_0 \frac{1 - \frac{\phi}{1 - \xi}}{\left(1 - \frac{\phi}{\phi_{\max}} \frac{1}{1 - \xi}\right)^2}$ (25)
Plastic viscosity	$\mu_p = \mu_p^0 \frac{1 - \frac{1 - \xi}{\phi}}{\left(1 - \frac{\phi}{\phi_{\max}} \frac{1}{1 - \xi}\right)^2}$ (31)
	Evolution equations for internal microstructural yield parameters
Back strain tensor	$\dot{A} = \dot{\gamma}^p - (q A)^v \text{sign}(A) \dot{\gamma}^p $ (23)
Microstructural parameter	$\dot{\lambda} = \frac{1}{\tau_{th,y}} (1 - \lambda) - \beta_y \lambda \dot{\gamma}^p $ (27)
Normalized fractal connectivity	$\dot{\xi} = \frac{1}{\tau_{th,v}} (\xi^* - \xi) - \beta_v \xi \dot{\gamma}^p ^n$ (14)
	Model parameters
	$\mu_v, G, \mu_{p,0}, m, \tau_{th,v}, \beta_v, n, C_0, \tau_{th,y}, \beta_y, \xi^*, \phi_{\max}, k, q, v$

where μ_p^0 is the value of the viscosity at the WAT, immediately before any wax has crystallized.

c. *Summary of FIKH model.* For convenience, in Table I we summarize all the equations that define the FIKH framework including the kinematics and stress balance. Note that the evolution equations for the microstructural internal variables [Eqs. (23),(27), and (14)] are first order ODEs and need an initial condition to be solved; thus, we need to specify initial values for A , λ , and ξ . It is evident that such conditions depend on the initial state of the material; however, to provide some guidance we first note that A can vary between 0 and its steady state value $1/q$, while the structural parameters vary between 0 and 1 (keeping in mind the discussion on ξ^*). As an example, following shear rejuvenation at $\dot{\gamma}$, a good set of initial values for (A, λ, ξ) is $(1/q, \lambda_{ss}(\dot{\gamma}), \xi_{ss}(\dot{\gamma}))$ (see Appendix C for further details).

With the linear viscoelastic Maxwell element and given that the actual volume fraction $\phi(T)$ is a known measurable function, the model introduces 15 unknown parameters: k , C_0 , $\mu_{p,0}$, m , μ_v , G , q , ν , $\tau_{th,y}$, β_y , $\tau_{th,v}$, β_v , n , ξ^* , ϕ_{\max} . Of these variables, many are easily determined by direct measurements, in particular.

- $\mu_{p,0}$ is the viscosity at the WAT that one can read directly from a temperature ramp;
- m is the slope of the flow curve at high shear rates;
- k is the static yield stress [given that $\max(\lambda) \rightarrow 1$];
- ϕ_{max} and C_0 can be easily set by following the approach we described in Sec. IV A 2 even with measurements of the viscosity and dynamic yield stress at only three or four different temperatures;
- ξ^* can be assumed as first approximation to be simply $\xi^* = 1 - \phi(T)/\phi_{max}$;
- G and μ_v can be set by small amplitude oscillatory shear experiments, probing the material at stresses below the static yield stress;
- $C(T, \xi)/q$, at a given temperature, is equal to the dynamic yield stress.

Although the number of parameters may appear large, it compares favorably to the available constitutive equations that attempt to capture thixotropy, temperature, and viscoelasticity at the same time [55,58,122]. This advantage remains also in the three-dimensional version since there would be no change in the total number of material constants and internal variables.

C. Experimental validation and predictions

The FIKH model is a complete constitutive framework that can be used with different shear and thermal histories. Although we have seen in Sec. IV A that the theory agrees very well with experiments, both in terms of thermal effects and thixotropic viscosity evolution under steady shear, we aim to show that the FIKH model is ultimately able not only to provide a good fit to data, but most importantly to *predict* the rheological response for different deformation histories. To this end, we performed a series of model simulations of our experimental results, focusing in particular on those that have not been used directly to test the goodness of the model. More specifically, we consider the experiments on irreversible destructuring that occur upon increasing the maximum shear rate that the material experiences, which are shown in Fig. 3(b) and discussed in Sec. II B 3.

In the simulations, we use the parameters derived from the determination of the plastic flow master curve and from the rejuvenation experiments. To obtain the other values, we proceeded similarly to what is suggested for the isothermal IKH model [56], so we primarily use the flow curve at 26 °C from Fig. 2(b). A procedure for fitting the IKH model to rheological experiments has already been presented [56] and therefore we do not reiterate the details here. Nevertheless, we point out that although the steady state flow curve at constant temperature can easily provide many parameters, in order to obtain a robust determination of certain quantities, especially those involved in the evolution equations for $A(t)$ and $\lambda(t)$ (i.e., q , β_y , $\tau_{th,y}$), one needs to perform transient experiments such as startup of shear or, better, LAOS tests at the same temperature. A quantitative example of how the different parameters affect LAOS transient curves can be found in the supplementary material of reference [56]. A detailed explanation of the fitting procedure for ξ and its evolution equation has been already elucidated in great detail

in Secs. IV A 2 and IV A 3. In general, we find that fitting the parameter values from a specific test sequence (such as that presented in this paper and in [56]) leads to an estimation which is physically meaningful and internally consistent, to the extent that even *prediction* of separate experimental observations can be achieved.

The final values of the parameters used in the numerical computations below and determined as discussed above, without a global optimization procedure, are the following: $k = 2.5$ Pa, $C_0 = 10$ Pa, $\mu_{p,0} = 0.1$ Pa s^m, $\mu_v = 500$ Pa s, $G = 250$ Pa, $q = 75$, $\nu = 0.25$, $\tau_{th,y} = 10$ s, $\beta_y = 10$, $\tau_{th,v} = 460$ s, $\beta_v = 3.2 \times 10^{-4}$ sⁿ⁻¹, $n = 0.24$, and $\phi_{max} = 0.28$. The simulations were performed by fixing the temperature at $T = 26$ °C and using, for each shear rate, the corresponding value of normalized fractal connectivity at the end of the rejuvenation step. The other internal variables, λ and A , were set to their steady state values. We used MATLAB® to solve the differential equations of our model including the constitutive equations for the LVE element. For each point in the $(\dot{\gamma}, \sigma)$ space, the simulation is run for a time of $(9\tau_{th,y})$ s, which corresponds to the first measurement that the rheometer provides.

Implementing this procedure leads to the results shown in Fig. 10(a), which are in very good agreement with the experimental results shown in Fig. 3(b). To quantify this, we provide direct comparison for three of the data sets in Fig. 10(b). Using parameter values that have all been independently determined from other experiments, we are able to quantitatively predict the measured rheological response and, in particular, the model is able to account for the apparent kinematic irreversibility that has been long observed in these waxy systems. The difference in each curve results from the different values of the normalized fractal connectivity and the irreversibility arises because, as we increase the maximum imposed shear rate, the radius of gyration of the fractal clusters decreases [according to the rate-dependent equilibrium solution of Eq. (14)] leading to a lower apparent viscosity [via Eq. (31)] and a less connected network with proportionally lower dynamic yield stress [through Eq. (27)]. As the shear rate is decreased (in the sweep down from the maximum shear rate), the dimension of the clusters does not recover completely because of the very long thixo-viscous time scale compared to the measurement time ($\tau_{exp}/\tau_{th,v} = 0.2 \ll 1$).

To demonstrate the quantitative fidelity of the FIKH model, we also performed simulations of the flow curves measured at each of the temperatures investigated in the experiments (see Appendix A), most of which are plotted in Fig. 10(c). In Fig. 10(d), we show a direct comparison of the experimental data with simulations for three different temperatures (below the WAT) corresponding to actual wax volume fractions of about 0.04%, 0.06%, and 0.08%, from the highest to the lowest values of T_f , respectively. For all three cases, the agreement with experiments is very good in the stable plastic flow region. The same framework can also be used to predict the mechanical response of the material in different flows, including thixotropic loops at different ramp speeds $(d\dot{\gamma}/dt)$, startup of steady shear or creep tests. The predictions for such protocols are shown in Appendix D. The results suggest that the FIKH model (summarized in Table I) captures many of the physical

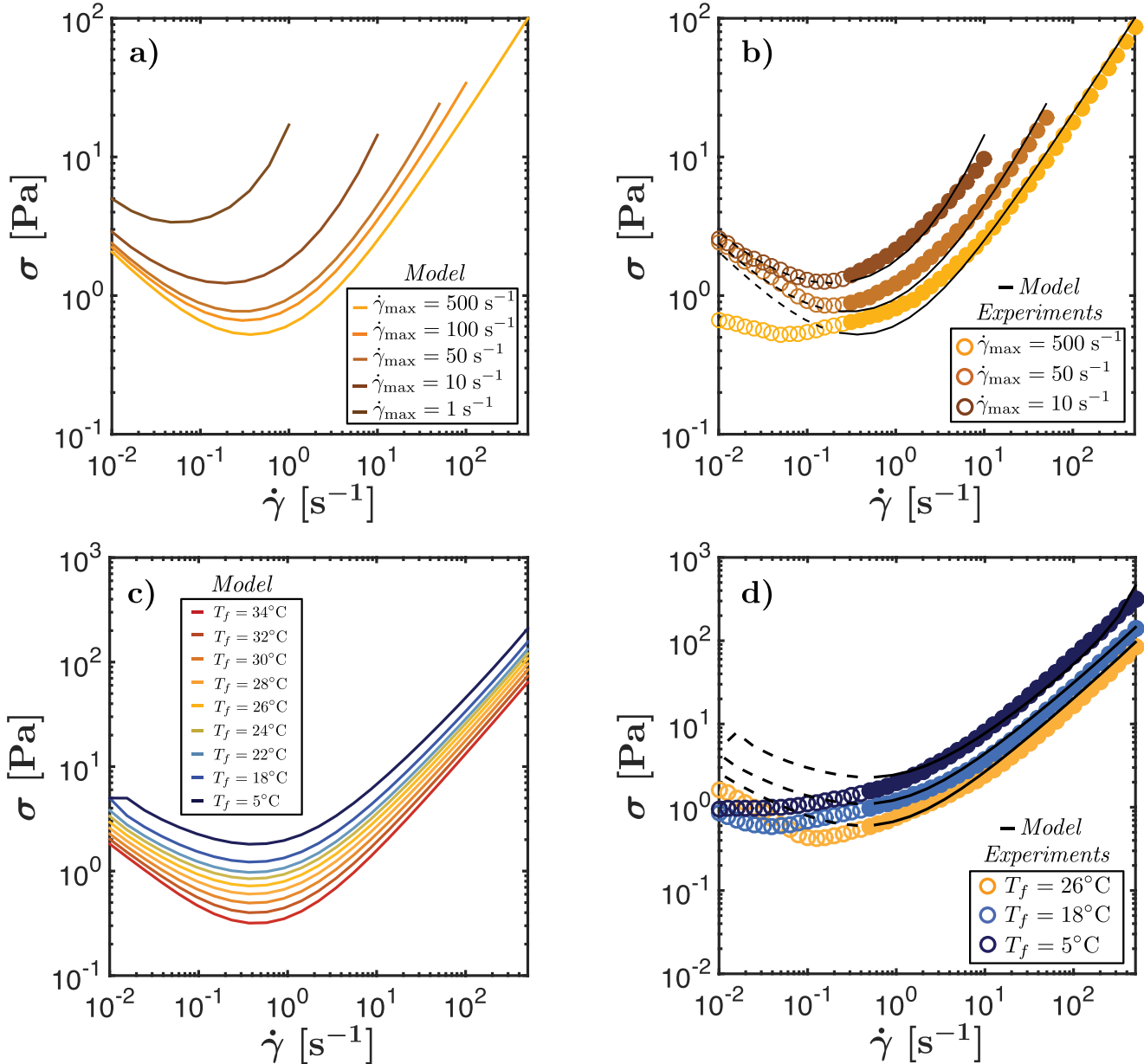


FIG. 10. (a) Simulations of the experimental data shown in Fig. 3(b) obtained using the FIKH model. Values of the parameters are the same as those shown in Fig. 8. The model is able to capture the irreversible destructuring that has been observed in such systems by accounting for the effect of the maximum shear rate on the aggregate size; (b) direct comparison of the experimental data of Fig. 3(b) (symbols) with the model predictions (black lines). The agreement is very good in the region where the flow is stable (closed symbols, solid lines); (c) simulations of the flow curves at different temperatures keeping all parameter values as in part (a) and (b) (complete set of experimental data shown in Appendix A). The effect of temperature can be captured by the FIKH model by using the appropriate value of actual volume fraction $\phi(T)$ determined from DSC experiments; (d) direct comparison of experiments and simulations for flow curves at three different temperatures performed with the same set of model parameters for the FIKH model as before. Predictions are in good agreement with experimental observations at all temperatures in the stable region of the flow curve (closed symbols, solid lines).

mechanisms which determine the complex rheological behavior of WCOs and for the first time it allows a description of the thermokinematic memory in these systems that is central to practical issues such as devising effective flow assurance strategies.

V. CONCLUSIONS AND FUTURE WORK

WCOs are a particular subset of the broader class of TEVP materials. Their rheological behavior is strongly affected not only by the shear history to which they are subject to, but also by the thermal history that they experience. Such

thermokinematic memory has posed a major challenge in fully understanding their behavior of such materials through rheological measurements because of the many difficulties in obtaining repeatable and consistent results. At the same time, the complexity of the material response has been hard to model with a comprehensive constitutive equation able to capture all of the different thermorheological features. In this work, we have shown that it is possible to make progress in understanding the rheology of WCOs by focusing sequentially on each of the physical mechanisms which give rise to their complex behavior. There are three major contributions of our study.

First, we presented a set of experimental protocols that can be used to consistently characterize the TEVP response of WCOs. These steps provide repeatable results and the ability to isolate many distinct features of the rheological behavior of WCOs by examining specific aspects of the steady state and transient response of the material. These experiments can be considered a nonisothermal extension to the canonical experiments suggested by Dimitriou and McKinley [56] for the isothermal characterization of WCOs.

Next, we elucidated the importance of a microstructural characterization in guiding our understanding of the experimental results. By directly accounting for the presence of fractal clusters of wax crystals and their interactions, we have been able to quantitatively describe both the role of temperature and the thixotropic nature of the plastic viscosity. As a result, we showed that the thermal material history is important, mainly in determining the amount of precipitated wax present in the system, but does not affect the way the crystals interact. The evolution of crystal aggregates under shear is instead what establishes the evolution in the viscoplastic material response.

Finally, we have presented a complete constitutive framework that can describe and predict the rheological measurements presented in this work as well as additional rheological test protocols (see Appendix D). The FIKH model extends the IKH model previously introduced to describe the isothermal rheology of WCOs by capturing the underlying fractal structure of the wax crystal clusters and the evolution of these aggregates under quiescent and flowing conditions, which leads to changes in the shape and size of the yield surface and magnitude of the plastic response above yield. This framework gives rise to a static and dynamic yield stress as well as three distinct time scales: A viscoelastic solid time scale (τ_{ve}), a thixo-plastic time scale for the evolution of the magnitude of the yield stress ($\tau_{th,y}$) as well as a thixo-viscous time scale ($\tau_{th,v}$) that describes the slow and rate-dependent evolution in size and shape of the fractal aggregates and sets the magnitude of the viscoplastic response during steady shear. Because the formulation of the FIKH framework is based on well-established principles in continuum plasticity, we expect it to be general enough that it can be adapted and applied to a range of different TEVP materials characterized by a similar underlying microstructure, i.e., solid non-Brownian interacting particles.

A one-dimensional form of the resulting constitutive model that is suitable for shearing deformations is described and has been solved for steady state shear flow as well as for transient protocols such as startup of steady shear and thixotropic loops. A complete three-dimensional, frame invariant, and thermodynamically consistent version of the FIKH model is presently being developed, which enables simulation of more complex flow and thermal histories that are typical of flow assurance strategies.

ACKNOWLEDGMENTS

M.G. and G.H.M. would like to acknowledge Chevron Technology Company for their on-going financial support.

M.G. and G.H.M. gratefully acknowledge use of the calorimeter QA100 (TA Instruments) of the Laboratory for Advanced Materials (LAM) in the Department of Material Science and Engineering at MIT. M.G. would like to thank A. F. Schwartzman and G. P. Berera for their training and assistance with DSC measurements.

APPENDIX A: ADDITIONAL EXPERIMENTS ON TEMPERATURE EFFECTS

In Fig. 11, we collect the flow curves measured at all of the different final temperatures (T_f) investigated in this work. Of the twelve temperatures at which measurements were performed, only $T_f = 40^\circ\text{C}$ is above the WAT ($T_{wa} = 37^\circ\text{C}$). As explained in the text, we can see that the behavior is purely Newtonian above WAT, the stress being linear with the strain rate. Below T_{wa} , the model oil shows the EVP response described in detail in Sec. II B 1. This figure shows more directly that the observations made based on Fig. 2(b) hold true for all the other temperatures in the range $T_{min} \leq T \leq T_{wa}$. The lowest value of temperature investigated has been set to $T_{min} = 5^\circ\text{C}$ based on the sea floor temperature, which is of interest in the context of flow assurance. Measurements of the viscosity of the pure mineral oil (Sigma Aldrich, 330760) as a function of temperature have already been reported [56,61].

APPENDIX B: FRACTAL DIMENSION OF THE MODEL WCO

Several researchers have suggested in the past that the microstructure formed by crystallization in WCO be regarded as fractal in nature [39,53,123]. In particular, Gao *et al.* [123] measured directly the value of the fractal dimension D_f by using a box counting method on a series of images of real crude oils taken using microscopy. Other researchers have measured the fractal dimension by fitting rheological data to the theory for colloidal gels [39] or to an adaptation of the theory introduced by Snabre and Mills [54].

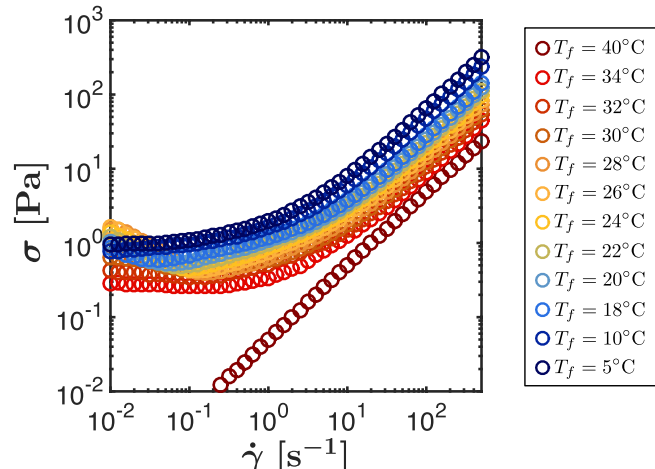


FIG. 11. Compilation of all the flow curves measured at twelve different final temperatures T_f defined as in Fig. 1. The waxy oil used is composed of 10 wt. % paraffin wax in heavy mineral oil as discussed in Sec. II A.

We have repeated a similar analysis on our model waxy oil. Figure 12 shows a series of pictures taken with the birefringence setup described in Sec. III (left column). The same images were converted into binary (right column) using the software IMAGEJ before being analyzed using the built-in box counting algorithm. The birefringence micrographs were taken on samples with different total wax contents (x_{tot}), respectively, 3, 5, and 10 wt. % from top to bottom, after they had been quenched to a final temperature $T_f = 25^\circ\text{C}$. The same trend is observed for a sample with a fixed total wax content, e.g., 10 wt. %, if quenched down to progressively lower final temperatures. Figure 13 shows the result of the box counting method applied to the three cases of Fig. 12. The trends suggest that, at least from analysis of 2D images, the fractal dimension increases as the temperature of

the sample decreases. A similar conclusion was obtained by Gao *et al.* [123] for samples of real WCO, with similar values of D_f .

This analysis has several limitations. First of all it deals only with a 2D projection of a 3D microstructure; therefore, the fractal dimension of true 3D structures might be different in value from the ones computed here. Also, it is extracted from images of a sample that has been quenched under static conditions and therefore does not account for the effect of shearing nor for changes due to slower cooling rates. However, these simple considerations offer a direct and quantitative support to our assumption that the microstructure formed below the WAT in crude oils is of fractal nature, with a fractal dimension D_f that can be computed using established methods.

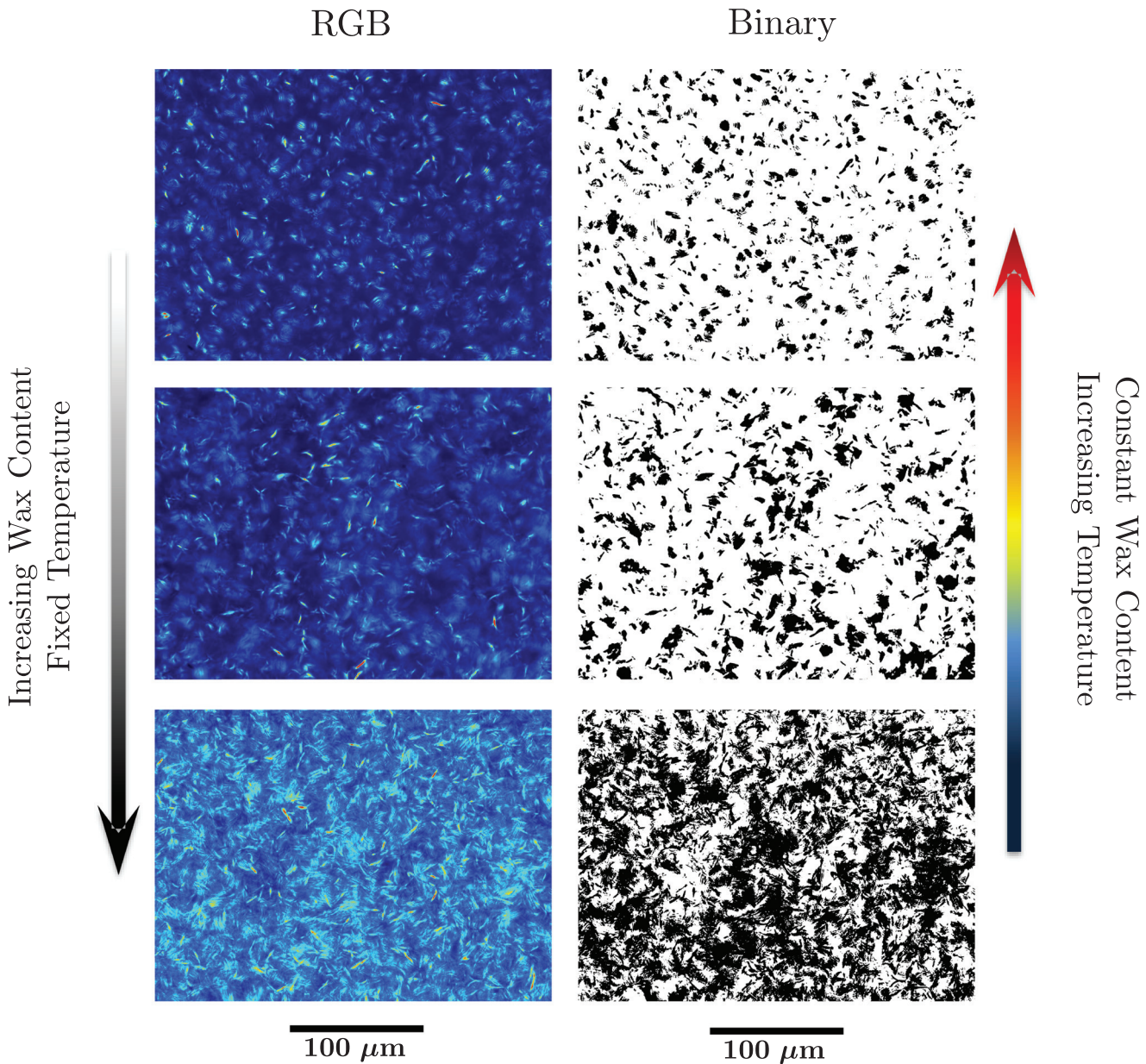


FIG. 12. 2D micrographs of the 3D model waxy oil microstructure taken using a birefringence microscope (left column) and processed into binary images (right column). The micrographs were taken on samples with different total wax contents, respectively, 3, 5, and 10 wt. % from top to bottom, after being cooled to a constant final temperature $T_f = 25^\circ\text{C}$. The same trend is observed for a sample with constant total wax content, i.e., 10 wt. %, but decreasing final temperatures.

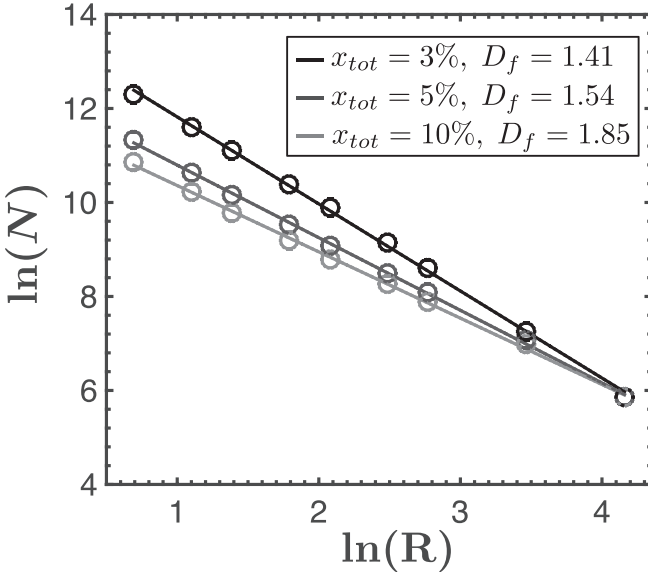


FIG. 13. Results from box counting method applied to the binary images shown in Fig. 12 using the software IMAGEJ (symbols). Lines are linear fitting to extract the corresponding fractal dimension (D_f).

APPENDIX C: HARDENING PROCESSES AND THE YIELD SURFACE

To properly describe the complex yielding mechanism experimentally observed for the model waxy oil, it is not sufficient to introduce a constant yield stress. Thixotropy, as well as the presence of a minimum in the flow curve, suggests that a more detailed description is required to capture all the interesting features. Dimitriou and coworkers [56,61] have shown that, by drawing on concepts already introduced in the plasticity literature [57,59], it is possible not only to develop a model that successfully describes the complex yield surface of WCOs but also to do so in a framework that is both thermodynamically consistent and frame invariant.

To this end, two hardening processes should be considered in the description of the yield surface: KH (or the Bauschinger effect) and IH. KH is a process that sees the locus of the yield stress surface moving in stress space without expanding or contracting. Such translation is associated with an accumulated stress in the microstructure, which reduces the effective stress the material can support before flowing plastically. This concept was first introduced in the plasticity literature to describe the mechanical response of polycrystalline metals (see for example [59,117,118] and references therein). For these materials, KH is due to dislocation-induced lattice deformations; when the deformation is large enough to be able to induce microstructural changes in the crystal lattice by allowing a flow of the dislocations toward grain boundaries and triple lines; on the macroscopic scale, the effect is hardening of the material. Part of the energy introduced during this process actively increases the free energy of the system by inducing a residual stress in the microstructure, called the back stress. To achieve steady plastic flow, a stress greater than this value has to be imposed; otherwise, plastic/inelastic deformation will occur until the microstructure has reconfigured and then no

additional creep will occur. In WCOs, and more generally in any suspension of attractive particles, reconfiguration of the microstructure arises from rearrangements of the interparticle contacts as well as the interaggregate contacts. KH has been shown to be effective in describing the hardening behavior of WCOs as well as different yield stress fluids under isothermal conditions [56,61], and this is especially evident in LAOS tests which cannot be correctly captured by any other scalar thixotropic model [122]. In fact, KH is associated, by definition, with a tensorial strainlike quantity (introduced in the text as **A**) that evolves based not only on the magnitude but also the direction of the applied deformation. In a one-dimensional model, such as that introduced in Sec. IV B, this tensorial variable reduces to a scalar with an associated sign ($\pm |A|$). Physical intuition suggests that in simulations, the initial value of A strongly depends on the type of history that the material has undergone. In general, one can set $A = 0$ if the material has been undeformed or has relaxed back to its original configuration (such as after an LAOS cycle). On the other hand, after a period of constant applied shear rate, $A = A_{ss}$ which in our case is always $A_{ss} = 1/q$ for Eq. (23) to hold. In fact, the evolution equation for A shows that under any applied plastic strain rate $\dot{\gamma}^p(t)$, even profiles that are not constant in magnitude but constant in the direction of flow, A evolves toward its steady state value $A_{ss} = 1/q$.

IH refers to a process for which the yield surface expands or contracts without changing its center. To describe such changes, it is sufficient to introduce a single positive scalar (which we have indicated by λ) that evolves both as a function of time and rate of deformation. As already discussed above, the microstructural parameter λ is normalized and generally varies between 0 and 1. The initial value $\lambda(t=0)$ used for performing simulations depends on the history of deformation before the initialization of computational time $t=0$. In general, if steady state can be assumed, the analytical solution for λ_{ss} can be easily used to obtain the initial condition for any subsequent applied shear rate

$$\lambda(t=0) = \lambda_{ss} = \frac{1}{1 + \beta_y \tau_{th,y} |\dot{\gamma}^p|}. \quad (C1)$$

It is worth mentioning here that an analogous discussion holds for the normalized fractal connectivity ξ with respect to its steady state value given in Eq. (17).

To show how these two processes are used to describe the yield surface of WCOs, here we provide a more detailed description of their contribution in determining the steady state flow curve of the model oil at constant temperature. Assuming that all the internal parameters have reached steady state and that the viscoelastic contribution to the shear rate is negligible compared to the plastic contribution (so that $\dot{\gamma} \simeq \dot{\gamma}^p$), an analytical expression for the shear stress as a function of the shear rate can be easily found in terms of the steady state values of the internal variables ($\phi(T)$, A_{ss} , λ_{ss} , and ξ_{ss}). Specifically

$$\sigma(\dot{\gamma}) = \mu_p(\xi_{ss}, T)\dot{\gamma}^m + \underbrace{C(\xi_{ss}, T)A_{ss}}_{\sigma_{back}} + \underbrace{k\lambda_{ss}}_{\sigma_y}, \quad (C2)$$

where we have highlighted the components coming from kinematic hardening and IH, respectively. The expression for the plastic viscosity, the back stress modulus, the steady state value of the normalized fractal connectivity, and the steady state value of the microstructural variable λ correspond to Eqs. (31), (25), (17), and (C1), respectively, while $A_{ss} = 1/q$. In Fig. 14(a), the total stress as well as the two hardening components are explicitly plotted in order to show how they contribute to the global mechanical response. The yield stress σ_y is directly proportional to $\lambda_{ss}(\dot{\gamma})$ through the modulus k , while the back stress as well as the plastic viscosity depends on the

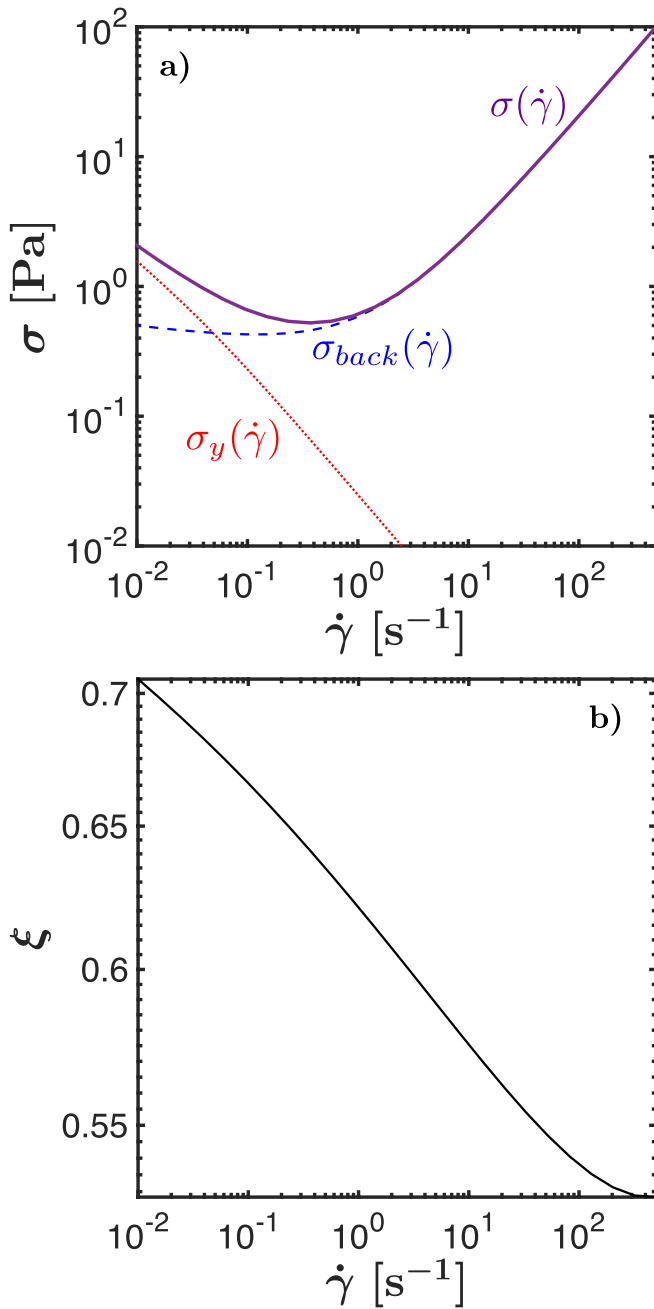


FIG. 14. (a) Steady state flow curve at $T = 26^\circ\text{C}$ obtained assuming $\dot{\gamma}_{cool} = 500 \text{ s}^{-1}$ (solid line). The contributions due to KH and IH are highlighted by the dashed line and dotted line, respectively; (b) Evolution of the normalized fractal connectivity as a function of the shear rate.

magnitude of the steady state normalized fractal connectivity that is plotted in Fig. 14(b) for the corresponding range of shear rates.

Figure 14(a) clearly shows that two distinct hardening mechanisms are necessary to capture both the dynamic yield stress, which corresponds to the back stress, and the static yield stress. The role of the back stress is of great importance especially when dealing with oscillating and reversing flows, where the direction of the deformation changes over time. Since A has a sign that can alternate based on the sign of the plastic shear rate as well as on its instantaneous magnitude $[A(t)]$, the value of the yield stress can be affected (either reduced or increased) depending on the shear history (magnitude and direction). Finally, it is important to note that at steady state the flow curve predicted by the model is effectively unique at each given temperature and does not depend on the shear history that the material has previously undergone. Differences in the apparent flow curve that can be measured with different protocols (see for example work by Divoux *et al.* [124]) are a consequence of the fact that the measured value of stress does not correspond to the equilibrium value of the underlying microstructure.

APPENDIX D: ADDITIONAL PREDICTIONS FROM FIKH MODEL

Having determined all the values of the model parameters, we can now use the FIKH framework to obtain the response of the model waxy oil to many different types of flow. Here, we show three additional predictions which are of great interest when dealing not only with WCOs but more generally with any thixotropic material: that is, thixotropic loops, startup of steady shear and creep tests.

In Fig. 15, we show the numerical results for two different thixotropic loops. The data have been obtained by simulating increasing and decreasing shear rate sweeps between two fixed shear rates ($\dot{\gamma}_{min} = 0.01 \text{ s}^{-1}$ and $\dot{\gamma}_{max} = 500 \text{ s}^{-1}$), varying the number of points per decade during one sweep (50 for the solid line and five for the dotted line). The time per point, that is the time during which a constant steady state is applied, has been kept constant in both cases and is equal to 10s; thus the total time per sweep in the two cases is $t_{tot} = 2250 \text{ s}$ and $t_{tot} = 220 \text{ s}$, respectively. Figure 15(a) shows the apparent flow curves measured during the numerical experiment. As expected, the cycle hysteresis is bigger for the case where the total time to perform one sweep is lower ($t_{tot} = 220 \text{ s}$). Interestingly though, the trend is reversed in the decreasing sweep for stresses between the dynamic yield stress and the static yield stress. To better understand these results, in Fig. 15(b), we plot the values of the microstructural parameter and of the normalized fractal connectivity. Their trends during the increasing and decreasing shear rate sweeps underpin the macroscopic response observed in terms of total shear stress. In particular, they show how the accumulated damage due to plastic deformation is always lower in the loop of shorter duration, except for very low shear rates during the decreasing portion of the hysteresis loop. In a fast thixotropic loop there is less time available for the sample to age at very low shear rates, which

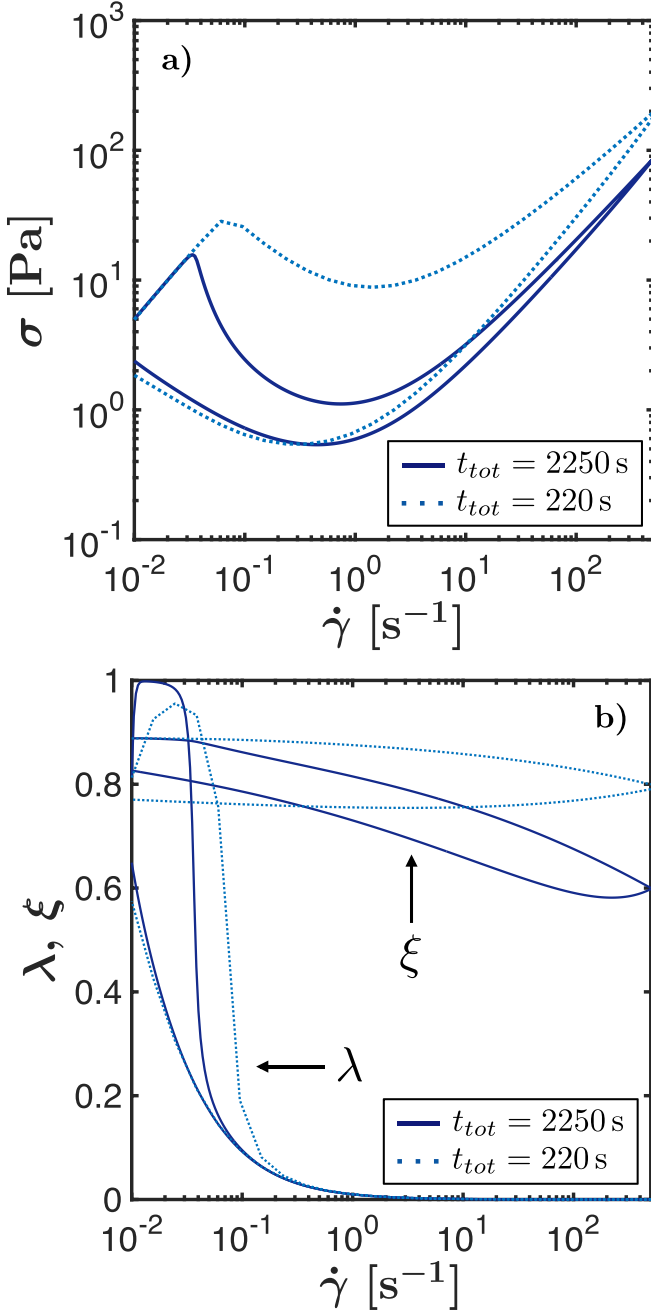


FIG. 15. (a) Simulation of thixotropic loop tests (increasing-decreasing shear rate sweeps) for the model waxy oil at $T = 30^\circ\text{C}$ obtained assuming $\dot{\gamma}_{cool} = 10^{-6}\text{ s}^{-1}$ and keeping $\dot{\gamma}_{max} = 500\text{ s}^{-1}$. Two cases are shown, as indicated in the legend, with different total time needed to perform one sweep (up or down); (b) evolution of the normalized fractal connectivity (ξ) and of the microstructural parameter (λ) as a function of the shear rate during the loop tests of part (a).

results in an effectively smaller level of IH. It is important to remember that, as anticipated before, the hysteresis is a consequence of the fact that the material is probed out of equilibrium and a unique steady state curve can be found if the sweeps are performed for a total time t_{tot} much greater than the longest time scale of the material (in this case $t_{tot} \gg \tau_{th,v}$).

In Fig. 16(a), we show the predictions for startup of steady shear. Simulations are performed for the standard protocol with $\dot{\gamma}_{cool} = 50\text{ s}^{-1}$ and different waiting times during which the sample is left unperturbed before applying a

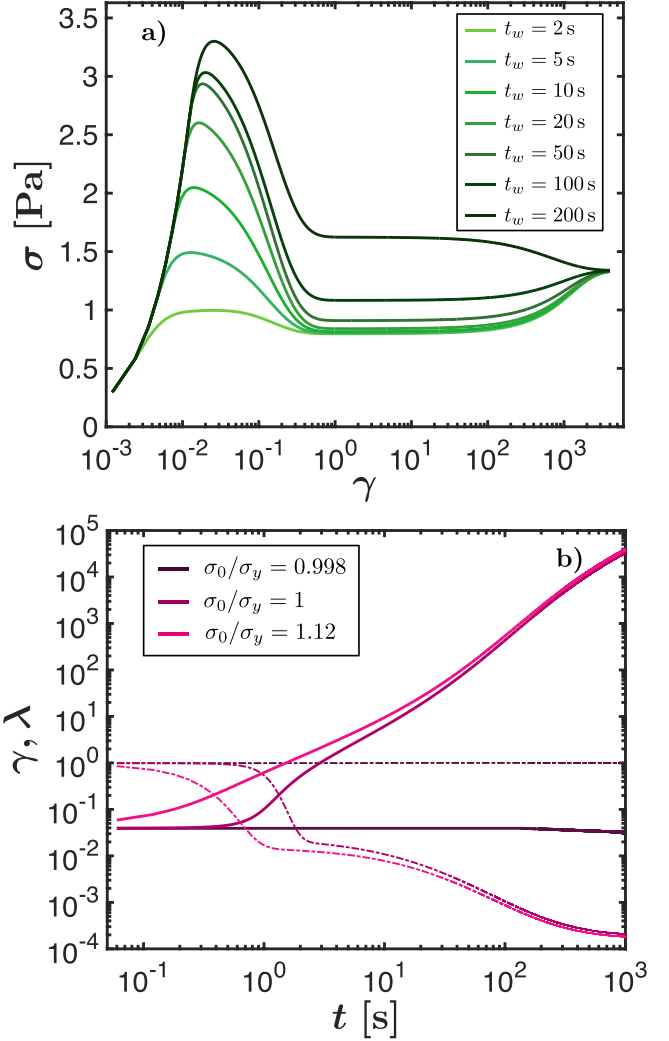


FIG. 16. (a) Simulations of startup of steady shear flow for the model waxy oil at $T = 26^\circ\text{C}$ obtained assuming $\dot{\gamma}_{cool} = 50\text{ s}^{-1}$ and imposing different waiting times; (b) simulations of creep tests close to the static yield stress value that show the ability of the FIKH model to capture delayed yielding. Details of the simulations are given in the text. Both the evolution of the strain (solid line) and of the microstructural parameter λ (dashed line) are shown. Colors represent different stresses as specified in the legend.

constant shear rate $\dot{\gamma} = 2\text{ s}^{-1}$ [56,61]. These results show the ability of the FIKH model to capture not only the overshoot but also an apparent plastic viscosity (at short times) that depends on the waiting time. However, as anticipated earlier, the steady state viscosity at very long times ($t \gg \tau_{th,v}$) is unique at a constant temperature and shear rate, and therefore, the final value of the stress eventually reaches the same plateau independently of the waiting time.

The trends displayed in Fig. 16(a) are important to show one possible issue with the assumption that ξ^* be equal to ξ_{max} [see discussion below Eq. (14)]. Due to the functional relation between the back modulus (C) and the normalized fractal connectivity (ξ), we can see that the simplified assumption on ξ^* leads to infinitely large values of the back stress for long waiting times, when $\xi \rightarrow \xi^*$, while a saturation value is expected. A similar issue arises for the plastic viscosity. These observations suggest that modifications to the assumption on ξ^* might be necessary, e.g., assuming ξ^* being a certain percentage of ξ_{max} , or that a slight

modification of the functional form for the back modulus and the plastic viscosity should be introduced to eliminate the slow mathematical divergence. However, given the very good agreement between experiments and theory for all the protocols shown in this work, we anticipate that such a modification should not significantly affect the proposed model.

Finally, in Fig. 16(b), we plot the response predicted by the FIKH model to creep tests when the imposed stress is very close to the value of the static yield stress. The set of parameters used is the same as for the previous simulations but a simple elastic spring is used in place of a Maxwell element, and the temperature has been set to $T = 30^\circ\text{C}$. Simulations were performed with an initial condition of steady state for the internal variables which corresponds to the material having reached equilibrium to a shear rate of about 10^{-4} s^{-1} , so that $A = 1/q$, $\lambda = 0.99$, and $\xi = 0.98\xi^*$. Using these conditions, neither the viscosity nor the back stress is infinitely large. With these parameter values, the static yield stress is about 9.82 Pa. Simulations show the evolution over time of both the strain (solid lines) and the microstructural parameter λ (dash-dot line) for different values of imposed stress, as indicated in the legend in a dimensionless form with respect to the static yield stress σ_y . The trends show clearly that close to the critical stress delayed yielding is obtained due to the evolution of the yield surface. For this set of parameters, the evolution of the viscosity and back stress is not appreciable with the achieved shear rates; however, for different materials, evolution in the viscosity or the back stress might be the dominant mechanism for delayed yielding. Under different loading protocols, avalanche behavior might also be achieved as a consequence of the nonmonotonic form of the flow curve, as already pointed out by Dimitriou and McKinley (see the supplementary material of [56]).

References

- [1] Oldroyd, J. G., "A rational formulation of the equations of plastic flow for a Bingham solid," *Math. Proc. Cambridge Philos. Soc.* **43**(1), 100–105 (1947).
- [2] Elliott, J. H., and C. E. Green, "Modification of food characteristics with cellulose hydrocolloids II: The modified Bingham body—A useful rheological model," *J. Texture Stud.* **3**(2), 194–205 (1972).
- [3] Rubin, M. B., "An elastic-viscoplastic model exhibiting continuity of solid and fluid states," *Int. J. Eng. Sci.* **25**(9), 1175–1191 (1987).
- [4] Isayev, A., and X. Fan, "Viscoelastic plastic constitutive equation for flow of particle filled polymers," *J. Rheol.* **34**(35), 35–54 (1990).
- [5] Doraiswamy, D., A. N. Mujumdar, I. Tsao, A. N. Beris, S. C. Danforth, and A. B. Metzner, "The Cox-Merz rule extended: A rheological model for concentrated suspensions and other materials with a yield stress," *J. Rheol.* **35**(4), 647–685 (1991).
- [6] Bauer, W. H., and E. A. Collins, "Thixotropy and dilatancy," in *Rheology, Theory and Applications* (Academic, New York and London, 1967), Vol. 4, Chap. 8, pp. 423–459.
- [7] Mewis, J., "Thixotropy—A general review," *J. Non-Newtonian Fluid Mech.* **6**(1), 1–20 (1979).
- [8] Barnes, H. A., "Thixotropy—A review," *J. Non-Newtonian Fluid Mech.* **70**(1–2), 1–33 (1997).
- [9] Mewis, J., and N. J. Wagner, "Thixotropy," *Adv. Colloid Interface Sci.* **147–148**, 214–227 (2009).
- [10] Möller, P., A. Fall, V. Chikkadi, D. Derk, and D. Bonn, "An attempt to categorize yield stress fluid behaviour," *Philos. Trans. Ser. A, Math. Phys. Eng. Sci.* **367**(1909), 5139–5155 (2009).
- [11] de Souza Mendes, P. R., "Thixotropic elasto-viscoplastic model for structured fluids," *Soft Matter* **7**(6), 2471–2483 (2011).
- [12] Coussot, P., A. Leonov, and J. Piau, "Rheology of concentrated dispersed systems in a low molecular weight matrix," *J. Non-Newtonian Fluid Mech.* **46**(2–3), 179–217 (1993).
- [13] Mujumdar, A., A. N. Beris, and A. B. Metzner, "Transient phenomena in thixotropic systems," *J. Non-Newtonian Fluid Mech.* **102**(2), 157–178 (2002).
- [14] de Souza Mendes, P. R., and R. L. Thompson, "A critical overview of elasto-viscoplastic thixotropic modeling," *J. Non-Newtonian Fluid Mech.* **187–188**, 8–15 (2012).
- [15] Dullaert, K., and J. Mewis, "A structural kinetics model for thixotropy," *J. Non-Newtonian Fluid Mech.* **139**(1–2), 21–30 (2006).
- [16] Cheng, D. C.-H., and F. Evans, "Phenomenological characterization of the rheological behaviour of inelastic reversible thixotropic and antithixotropic fluids," *Br. J. Appl. Phys.* **16**, 1599–1617 (1965).
- [17] Coussot, P., Q. D. Nguyen, H. T. Huynh, and D. Bonn, "Viscosity bifurcation in thixotropic, yielding fluids," *J. Rheol.* **46**(3), 573–589 (2002).
- [18] Coussot, P., "Rheophysics of pastes: A review of microscopic modelling approaches," *Soft Matter* **3**(5), 528–540 (2007).
- [19] de Souza Mendes, P. R., "Modeling the thixotropic behavior of structured fluids," *J. Non-Newtonian Fluid Mech.* **164**(1–3), 66–75 (2009).
- [20] Larson, R. G., "Constitutive equations for thixotropic fluids," *J. Rheol.* **59**(3), 595–611 (2015).
- [21] Sollich, P., F. Lequeux, P. Hébraud, and M. E. Cates, "Rheology of soft glassy materials," *Phys. Rev. Lett.* **78**(10), 2020–2023 (1997).
- [22] Sollich, P., "Rheological constitutive equation for a model of soft glassy materials," *Phys. Rev. E* **58**(1), 738–759 (1998).
- [23] Falk, M. L., and J. S. Langer, "Dynamics of viscoplastic deformation in amorphous solids," *Phys. Rev. E* **57**(6), 7192–7205 (1998).
- [24] Langer, J. S., and L. Pechenik, "Dynamics of shear-transformation zones in amorphous plasticity: Energetic constraints in a minimal theory," *Phys. Rev. E* **68**, 061507 (2003).
- [25] Bocquet, L., A. Colin, and A. Ajdari, "Kinetic theory of plastic flow in soft glassy materials," *Phys. Rev. Lett.* **103**(3), 036001 (2009).
- [26] Mansard, V., A. Colin, P. Chauduri, and L. Bocquet, "A kinetic elasto-plastic model exhibiting viscosity bifurcation in soft glassy materials," *Soft Matter* **7**(12), 5524–5527 (2011).
- [27] Goyon, J., A. Colin, G. Ovarlez, A. Ajdari, and L. Bocquet, "Spatial cooperativity in soft glassy flows," *Nature* **454**(7200), 84–87 (2008).
- [28] Goyon, J., A. Colin, and L. Bocquet, "How does a soft glassy material flow: Finite size effects, non local rheology, and flow cooperativity," *Soft Matter* **6**(12), 2668–2678 (2010).
- [29] Perkins, T. K., and J. B. Turner, "Starting behavior of gathering lines and pipelines filled with gelled Prudhoe bay oil," *J. Pet. Technol.* **23**, 301–308 (1971).
- [30] Chin, W. C., "Modern flow assurance methods: Clogged pipelines, wax deposition, hydrate plugs," *Offshore* **60**(9), 92–94 (2000).
- [31] Wardhaugh, L. T., and D. V. Boger, "Flow characteristics of waxy crude oils: Application to pipeline design," *AICHE J.* **37**(6), 871–885 (1991).
- [32] Venkatesan, R., and J. L. Creek, "Wax deposition and rheology: Progress and problems from an operator's view," in Offshore Technology Conference, Offshore Technology Conference (2010).
- [33] Cheng, D. C.-H., "Yield stress: A time-dependent property and how to measure it," *Rheol. Acta* **25**(5), 542–554 (1986).

- [34] Paso, K., T. Kompalla, H. J. Oschmann, and J. Sjöblom, "Rheological degradation of model wax-oil gels," *J. Dispersion Sci. Technol.* **30**, 472–480 (2009).
- [35] Asphaltenes, Heavy Oils, and Petroleomics, edited by O. C. Mullins, E. Y. Sheu, A. Hammami, and A. G. Marshall (Springer, New York, 2007).
- [36] Padgett, F. W., D. G. Hefley, and A. Henriksen, "Wax crystallization a preliminary report," *Ind. Eng. Chem. Fundam.* **18**(8), 832–835 (1926).
- [37] Edwards, R. T., "Crystal habit of paraffin wax," *Ind. Eng. Chem. Fundam.* **49**, 750–757 (1957).
- [38] Kané, M., M. Djabourov, J.-L. Volle, J.-P. Lechaire, and G. Frebourg, "Morphology of paraffin crystals in waxy crude oils cooled in quiescent conditions and under flow," *Fuel* **82**(2), 127–135 (2003).
- [39] Kané, M., M. Djabourov, and J.-L. Volle, "Rheology and structure of waxy crude oils in quiescent and under shearing conditions," *Fuel* **83**(11–12), 1591–1605 (2004).
- [40] Webber, R. M., "Low temperature rheology of lubricating mineral oils: Effects of cooling rate and wax crystallization on flow properties of base oils," *J. Rheol.* **43**(4), 911–931 (1999).
- [41] Paso, K. G., and H. S. Fogler, "Bulk stabilization in wax deposition systems," *Energy Fuels* **18**(4), 1005–1013 (2004).
- [42] Paso, K. G., M. Senra, Y. Yi, A. M. Sastry, and H. S. Fogler, "Paraffin polydispersity facilitates mechanical gelation," *Ind. Eng. Chem. Fundam. Res.* **44**(18), 7242–7254 (2005).
- [43] Petter Rønning, H., "Rheological behaviour of gelled, waxy North Sea crude oils," *J. Pet. Sci. Eng.* **7**(3–4), 177–213 (1992).
- [44] Speight, J. G., *The Chemistry and Technology of Petroleum*, 5th ed. (CRC, 2014).
- [45] Venkatesan, R., J.-A. Östlund, H. Chawla, P. Wattana, M. Nydén, and H. S. Fogler, "The effect of asphaltenes on the gelation of waxy oils," *Energy Fuels* **17**(6), 1630–1640 (2003).
- [46] Magda, J. J., H. El-Gendy, K. Oh, M. D. Deo, A. Montesi, and R. Venkatesan, "Time-dependent rheology of a model waxy crude oil with relevance to gelled pipeline restart," *Energy Fuels* **23**(3), 1311–1315 (2009).
- [47] Dimitriou, C. J., G. H. McKinley, and R. Venkatesan, "Rheo-PIV analysis of the yielding and flow of model waxy crude oils," *Energy Fuels* **25**(7), 3040–3052 (2011).
- [48] Mendes, R., G. Vinay, G. Ovarlez, and P. Coussot, "Reversible and irreversible destructuring flow in waxy oils: An MRI study," *J. Non-Newtonian Fluid Mech.* **220**, 77–86 (2015).
- [49] Dimitriou, C. J., "The rheological complexity of waxy crude oils: Yielding, thixotropy and shear heterogeneities," Ph.D. thesis, Massachusetts Institute of Technology, Cambridge, MA, 2013.
- [50] Houska, M., "Inzenýrske aspekty reologie tixotropních kapalin," Ph.D. thesis, Technical University of Prague, Praha, Czechia, 1980.
- [51] Pedersen, K. S., and H. P. Rønning, "Effect of precipitated wax on viscosity a model for predicting non-Newtonian viscosity of crude oils," *Energy Fuels* **14**(1), 43–51 (2000).
- [52] Visintin, R. F. G., R. Lapasin, E. Vignati, P. D'Antona, and T. P. Lockhart, "Rheological behavior and structural interpretation of waxy crude oil gels," *Langmuir* **21**(14), 6240–6249 (2005).
- [53] Palermo, T., and E. Tournis, "Viscosity prediction of waxy oils: Suspension of fractal aggregates (SoFA) model," *Ind. Eng. Chem. Fundam. Res.* **54**(16), 4526–4534 (2015).
- [54] Snabre, P., and P. Mills, "I. Rheology of weakly flocculated suspensions of rigid particles," *J. Phys. III France* **6**(12), 1811–1834 (1996).
- [55] Mendes, R., G. Vinay, G. Ovarlez, and P. Coussot, "Modeling the rheological behavior of waxy crude oils as a function of flow and temperature history," *J. Rheol.* **59**(3), 703–732 (2015).
- [56] Dimitriou, C. J., and G. H. McKinley, "A comprehensive constitutive law for waxy crude oil: A thixotropic yield stress fluid," *Soft Matter* **10**(35), 6619–6644 (2014).
- [57] Anand, L., and C. Su, "A constitutive theory for metallic glasses at high homologous temperatures," *Acta Mater.* **55**(11), 3735–3747 (2007).
- [58] Anand, L., N. M. Ames, V. Srivastava, and S. A. Chester, "A thermomechanically coupled theory for large deformations of amorphous polymers. Part I: Formulation," *Int. J. Plast.* **25**(8), 1474–1494 (2009).
- [59] Gurtin, M. E., E. Fried, and L. Anand, *The Mechanics and Thermodynamics of Continua* (Cambridge University, Cambridge, 2010).
- [60] Webber, R. M., "Yield properties of wax crystal structures formed in lubricant mineral oils," *Ind. Eng. Chem. Fundam. Res.* **40**(1), 195–203 (2001).
- [61] Dimitriou, C. J., R. H. Ewoldt, and G. H. McKinley, "Describing and prescribing the constitutive response of yield stress fluids using large amplitude oscillatory shear stress (LAOSstress)," *J. Rheol.* **57**(1), 27–70 (2013).
- [62] Rogers, S. A., P. T. Callaghan, G. Petekidis, and D. Vlassopoulos, "Time-dependent rheology of colloidal star glasses," *J. Rheol.* **54**(1), 133–158 (2010).
- [63] E. N. da C. Andrade, "The viscosity of liquids," *Nature* **125**, 309–310 (1930).
- [64] E. N. da C. Andrade, "Viscosity of liquids," *Proc. R. Soc. Lond. Math. Phys. Sci.* **215**(1120), 36–46 (1952).
- [65] Lorge, O., M. Djabourov, and F. Brucy, "Crystallisation and gelation of waxy crude oils under flowing conditions," *Rev. Inst. Fr. Pét.* **52**(2), 235–239 (1997).
- [66] Coussot, P., *Rheometry of Pastes, Suspensions, and Granular Material* (John Wiley & Sons, Inc., Hoboken, 2005).
- [67] Fielding, S. M., "Complex dynamics of shear banded flows," *Soft Matter* **3**(10), 1262–1279 (2007).
- [68] Möller, P. C. F., J. Mewis, and D. Bonn, "Yield stress and thixotropy: On the difficulty of measuring yield stresses in practice," *Soft Matter* **2**(4), 274–283 (2006).
- [69] Berret, J.-F., "Transient rheology of wormlike micelles," *Langmuir* **13**(8), 2227–2234 (1997).
- [70] Michel, E., J. Appell, F. Molino, J. Kieffer, and G. Porte, "Unstable flow and nonmonotonic flow curves of transient networks," *J. Rheol.* **45**(6), 1465–1477 (2001).
- [71] Olmsted, P. D., "Perspectives on shear banding in complex fluids," *Rheol. Acta* **47**(3), 283–300 (2008).
- [72] Rogers, S. A., D. Vlassopoulos, and P. T. Callaghan, "Aging, yielding, and shear banding in soft colloidal glasses," *Phys. Rev. Lett.* **100**(12), 128304 (2008).
- [73] Möller, P. C. F., S. Rodts, M. A. J. Michels, and D. Bonn, "Shear banding and yield stress in soft glassy materials," *Phys. Rev. E* **77**(4 Pt 1), 041507 (2008).
- [74] Dijksman, J. A., G. H. Wortel, L. T. H. van Dellen, O. Dauchot, and M. van Hecke, "Jamming, yielding, and rheology of weakly vibrated granular media," *Phys. Rev. Lett.* **107**(10), 108303 (2011).
- [75] Pignon, F., "Thixotropic colloidal suspensions and flow curves with minimum: Identification of flow regimes and rheometric consequences," *J. Rheol.* **40**(4), 573–587 (1996).
- [76] Gibaud, T., C. Barentin, and S. Manneville, "Influence of boundary conditions on yielding in a soft glassy material," *Phys. Rev. Lett.* **101**(25), 258302 (2008).
- [77] Gibaud, T., C. Barentin, N. Taberlet, and S. Manneville, "Shear-induced fragmentation of Laponite suspensions," *Soft Matter* **5**(16), 3026–3037 (2009).

- [78] Geri, M., B. Saint-Michel, T. Divoux, S. Manneville, and G. H. McKinley, "Insights on the local dynamics during transient flows of waxy crude oils," *Bull. Am. Phys. Soc.* **60**(21) (2015).
- [79] Singh, P., H. S. Fogler, and N. Nagarajan, "Prediction of the wax content of the incipient wax-oil gel in a pipeline: An application of the controlled-stress rheometer," *J. Rheol.* **43**(6), 1437–1459 (1999).
- [80] Rhodes, F. H., C. W. Mason, and W. R. Sutton, "Crystallization of paraffin wax," *Ind. Eng. Chem. Fundam.* **19**(8), 935–938 (1927).
- [81] Ferris, S. W., "Crystal behavior of paraffin wax," *Ind. Eng. Chem. Fundam.* **37**(11), 1054–1062 (1945).
- [82] Venkatesan, R., N. Nagarajan, K. Paso, Y.-B. Yi, A. Sastry, and H. Fogler, "The strength of paraffin gels formed under static and flow conditions," *Chem. Eng. Sci.* **60**(13), 3587–3598 (2005).
- [83] Létoffé, J. M., P. Claudy, M. Garcin, and J. L. Volle, "Evaluation of crystallized fractions of crude oils by differential scanning calorimetry," *Fuel* **74**(1), 92–95 (1995).
- [84] Kané, M., M. Djabourov, J. L. Volle, and D. N. Rutledge, "Correction of biased time domain NMR estimates of the solid content of partially crystallized systems," *Appl. Magn. Reson.* **22**(3), 335–346 (2002).
- [85] Chen, J., J. Zhang, and H. Li, "Determining the wax content of crude oils by using differential scanning calorimetry," *Thermochim. Acta* **410**, 23–26 (2004).
- [86] Gill, P., T. T. Moghadam, and B. Ranjbar, "Differential scanning calorimetry techniques: Applications in biology and nanoscience," *J. Biomol. Tech.* **21**(4), 167–193 (2010).
- [87] Bosq, N., E. Zhuravlev, and N. Sbirrazzuoli, "Nonisothermal crystallization of polytetra fluoroethylene in a wide range of cooling rates," *J. Phys. Chem. B* **117**, 3407–3415 (2013).
- [88] Vyazovkin, S., K. Chrissafis, M. L. Di Lorenzo, N. Koga, M. Pijolat, B. Roduit, N. Sbirrazzuoli, and J. J. Suñol, "ICTAC kinetics committee recommendations for collecting experimental thermal analysis data for kinetic computations," *Thermochim. Acta* **590**, 1–23 (2014).
- [89] Mohraz, A., and M. J. Solomon, "Orientation and rupture of fractal colloidal gels during start-up of steady shear flow," *J. Rheol.* **49**(3), 657–681 (2005).
- [90] Vyazovkin, S., A. K. Burnham, J. M. Criado, L. A. Pérez-Maqueda, C. Popescu, and N. Sbirrazzuoli, "ICTAC kinetics committee recommendations for performing kinetic computations on thermal analysis data," *Thermochim. Acta* **520**(1–2), 1–19 (2011).
- [91] Danley, R. L., "New heat flux DSC measurement technique," *Thermochim. Acta* **395**, 201–208 (2003).
- [92] Mullins, O. C., "The asphaltenes," *Annu. Rev. Anal. Chem. (Palo Alto, Calif.)* **4**, 393–418 (2011).
- [93] Bird, R. B., R. C. Armstrong, and O. Hassager, *Dynamics of Polymeric Liquids. I: Fluid Mechanics*, 2nd ed. (John Wiley and Sons Inc., New York, 1987).
- [94] Einstein, A., "A new determination of the molecular dimensions," *Ann. Phys.* **19**(2), 591–592 (1906).
- [95] Frankel, N., and A. Acrivos, "On the viscosity of a concentrated suspension of solid spheres," *Chem. Eng. Sci.* **22**, 847–853 (1967).
- [96] Batchelor, G. K., "The effect of Brownian motion on the bulk stress in a suspension of spherical particles," *J. Fluid Mech.* **83**(1), 97–117 (1977).
- [97] Brady, J. F., A. S. Khair, and M. Swaroop, "On the bulk viscosity of suspensions," *J. Fluid Mech.* **554**, 109–123 (2006).
- [98] Krieger, I. M., and T. J. Dougherty, "A mechanism for non-Newtonian flow in suspensions of rigid spheres," *J. Rheol.* **3**(1), 137–152 (1959).
- [99] Cross, M. M., "Rheology of non-Newtonian fluids: A new flow equation for pseudoplastic systems," *J. Colloid Sci.* **20**(5), 417–437 (1965).
- [100] Quemada, D., and C. Berli, "Energy of interaction in colloids and its implications in rheological modeling," *Adv. Colloid Interface Sci.* **98**(1), 51–85 (2002).
- [101] Mills, P., "Non-Newtonian behaviour of flocculated suspensions," *J. Phys. Lett.* **46**(7), 301–309 (1985).
- [102] Wildemuth, C. R., and M. C. Williams, "Viscosity of suspensions modeled with a shear-dependent maximum packing fraction," *Rheol. Acta* **23**(6), 627–635 (1984).
- [103] Hausdorff, F., "Dimension und äußeres Maß," *Math. Ann.* **79**(1–2), 157–179 (1918).
- [104] Genovese, D. B., "Shear rheology of hard-sphere, dispersed, and aggregated suspensions, and filler-matrix composites," *Adv. Colloid Interface Sci.* **171–172**, 1–16 (2012).
- [105] Mathew, M., T. Schilling, and M. Oettel, "Connectivity percolation in suspensions of hard platelets," *Phys. Rev. E—Stat. Nonlinear Soft Matter Phys.* **85**(6), 1–7 (2012).
- [106] Wessel, R., and R. C. Ball, "Fractal aggregates and gels in shear flow," *Phys. Rev. A* **46**, R3008(R) (1992).
- [107] Moore, F., "The rheology of ceramic slips and bodies," *Trans. Br. Ceram. Soc.* **58**, 470–494 (1959).
- [108] Goodeve, C., and G. Whitfield, "The measurement of thixotropy in absolute units," *Trans. Faraday Soc.* **34**, 511–520 (1938).
- [109] Coleman, B. D., and W. Noll, "The thermodynamics of elastic materials with heat conduction and viscosity," *Arch. Ration. Mech. Anal.* **13**(1), 167–178 (1963).
- [110] Henann, D. L., and L. Anand, "A large deformation theory for rate-dependent elastic-plastic materials with combined isotropic and kinematic hardening," *Int. J. Plast.* **25**(10), 1833–1878 (2009).
- [111] Onsager, L., "Reciprocal relations in irreversible processes. I," *Phys. Rev.* **37**, 405–426 (1931).
- [112] Onsager, L., "Reciprocal relations in irreversible processes. II," *Phys. Rev.* **38**, 2265–2279 (1931).
- [113] Beris, A. N., and B. J. Edwards, *Thermodynamics of Flowing Systems with Internal Microstructure* (Oxford University, New York, 1994).
- [114] Grmela, M., and H. Öttinger, "Dynamics and thermodynamics of complex fluids. I. Development of a general formalism," *Phys. Rev. E* **56**(6), 6620–6632 (1997).
- [115] Öttinger, H. C., and M. Grmela, "Dynamics and thermodynamics of complex fluids. II. Illustrations of a general formalism," *Phys. Rev. E* **56**(6), 6633–6655 (1997).
- [116] Prager, W., "The theory of plasticity: A survey of recent achievements," *Proc. Inst. Mech. Eng.* **169**, 41–57 (1955).
- [117] Lion, A., "Constitutive modelling in finite thermoviscoelasticity: A physical approach based on nonlinear rheological models," *Int. J. Plast.* **16**, 469–494 (2000).
- [118] Anand, L., and C. Su, "A theory for amorphous viscoplastic materials undergoing finite deformations, with application to metallic glasses," *J. Mech. Phys. Solids* **53**(6), 1362–1396 (2005).
- [119] Mewis, J., "On the need for multi-parameter theories in the analysis of thixotropic behaviour," *J. Phys. D: Appl. Phys.* **8**(12), L148–L151 (1975).
- [120] Mewis, J., A. J. B. Spaull, and J. Helsen, "Structural hysteresis," *Nature* **253**, 618–619 (1975).
- [121] von Prandtl, L., "Spannungsverteilung in plastischen Körpern," in *Proceedings 1st International Congress on Applied Mechanics, Delft*, edited by C. Biezeno and J. Burgers (J. Waltman, Delft, 1925), pp. 43–54.
- [122] M. J. Armstrong, A. N. Beris, S. A. Rogers, and N. J. Wagner, "Dynamic shear rheology of a thixotropic suspension: Comparison of an improved structure-based model with large amplitude oscillatory shear experiments," *J. Rheol.* **60**(3), 433–450 (2016).
- [123] Gao, P., J. Zhang, and G. Ma, "Direct image-based fractal characterization of morphologies and structures of wax crystals in waxy crude oils," *J. Phys.: Condens. Matter* **18**(50), 11487–11506 (2006).
- [124] Divoux, T., V. Grenard, and S. Manneville, "Rheological hysteresis in soft glassy materials," *Phys. Rev. Lett.* **110**(1), 1–5 (2013).